Interannual variability of chlorofluorocarbons, pCFC ages and ideal ages in the North Pacific from 1958-2000 as simulated by an ocean general circulation model

Daisuke Tsumune
Environment Science Research Laboratory
Central Research Institute of Electric Power Industry (CRIEPI)
Abiko, Chiba, JAPAN

Frank O. Bryan
Climate and Global Dynamics
National Center for Atmospheric Research
Boulder, CO USA

Scott C. Doney
Marine Chemistry and Geochemistry
Woods Hole Oceanographic Institution
Woods Hole, MA USA

Matthew W. Hecht
Computer and Computational Sciences Division
Los Alamos National Laboratory
Los Alamos, NM USA

Abstract

Chlorofluorocarbon (CFCs) concentrations and ideal age are simulated in a global integration of the Parallel Ocean Program (POP) with realistic surface forcing derived from the NCEP/NCAR reanalysis (1958-2000). The present study focuses on the subtropical and subpolar thermocline of the North Pacific due to the relatively good observational coverage and the well documented decadal timescale variability of the circulation for that region. Tracer ventilation ages are computed from the simulation using the CFC partial pressure (pCFC). Biases arise in pCFC ages due to the interaction of mixing with the non-linear CFC atmospheric time-histories, and the model CFC ages significantly underestimate ideal age in the mid- to lower-thermocline and in the shadow zone of the eastern tropics and subtropics. Variability in pCFC ages is well correlated with variability of ideal age on interannual timescales, though the amplitude of the pCFC variability may be substantially less due to the offsets between the tracer and ideal ages and their spatial gradients. Over much of the subtropical gyre, age variability is also well correlated with that of potential vorticity. The significant interannual variability in tracer ages and longer-term temporal trends in the tracer age biases complicate the interpretation of CFC data collected from repeat occupations on 5 to 10 year intervals as currently envisioned by CLIVAR. In particular, the tracer age differences from the instantaneous samples are likely not representative, at least directly,

of interdecadal variability in ocean ventilation.

1. Introduction

Transient chemical tracers such as ^{3}H, ^{3}He, chlorofluorocarbons, and radiocarbon (^{14}C) are used extensively in oceanography to constrain the pathways, mechanisms, and rates of ocean circulation. The two chlorofluorocarbons, CFC-11 and CFC-12 are particularly useful in this regard because they have no natural sources, are essentially inert in seawater, and have relatively well known atmospheric time histories [*Bullister*, 1989]. One key application is to quantify ventilation ages, commonly defined as the time elapsed since a parcel was last in contact with the atmosphere. CFC based tracer ages are used routinely to characterize thermocline circulation [e.g., *Warner et al*., 1996] and infer biogeochemical cycling, for example the amount of anthropogenic CO_2 in the ocean [*Gruber et al.,* 1996] and oxygen utilization rates [e.g., *Sonnerup et al*., 1999]. As more measurements become available, especially from reoccupations of stations or sections, temporal changes in CFC concentrations and tracer ages also offer indices of interannual to decadal variability in water mass formation and circulation [*Doney et al.,* 1998a, *Watanabe et al.,* 2002; *Mecking et al.,* 2004a]. Here, we present and analyze simulated time-evolving ocean CFC concentration fields from a model driven by realistic historical forcing where our primary focus is on determining the usefulness of CFC and CFC age field data as quantitative measures of inter-annual to decadal timescale variability of ventilation.

The so-called pCFC (partial pressure) tracer-age approach takes advantage of the fact that atmospheric CFC-11 and CFC-12 concentrations grew monotonically until the early to late 1990's, thus providing a unique "time stamp" for subsurface waters [*Doney and Bullister*, 1992]. CFC concentration of a water sample is first transformed into a partial pressure (pCFC) with a temperature and salinity dependent solubility function [*Warner and Weiss*, 1985]. The most recent time of ventilation is found by matching the observed pCFC value to the atmospheric time history (Figure 1), assuming full solubility equilibrium. Age is derived by difference from the sampling date. CFC age estimates are practical but imperfect proxies for true "ideal" age, which would be the (immeasurable) weighted average of the ventilation ages for all of the various components/pathways that contribute to individual water parcels [*England*, 1995].

Biases in the CFC ages arise because of the interaction of ocean mixing with non-linearity (positive/negative curvature) in the atmospheric CFC time-histories (Figure 1), and CFC age distributions can change over time even under steady transport [*Doney et al.,* 1997]. The relationship between CFC age and ideal age has been determined empirically using simple one-dimensional advection-diffusion models [*Sonnerup*, 2001], idealized and realistic two-dimensional models [*Doney et al*., 1997; *Mecking et al*., 2004b], and the formalism of transit time distributions [*Waugh et al*., 2003]. For older, deeper waters and areas where mixing is significant relative to direct, advective ventilation, pCFC ages tend to underestimate ideal age because of the positive curvature of most of the atmospheric time history and because of the incorporation of CFC free waters that pre-date the CFC transient. *Sonnerup* [2001], for example, found that pCFC

ages could underestimate ideal age by more than a factor of four, with the error increasing with age and with the importance of mixing relative to advection in the net tracer transport. After the early- 1990's, however, age overestimates are also possible due to the change in sign of the atmospheric time curvature (Figure 1). *Holzer and Hall* [2000] and *Haine and Hall* [2002] highlight the fact that any single age measure is an imperfect estimate of the actual ventilation age within any particular water parcel when mixing is present. These effects can obscure the attribution of changes in estimated age to changes in ocean circulation and ventilation rates resulting from forced or intrinsic variability.

Because the pathways of CFC thermocline ventilation are similar to those of oxygen, CFCs are quite useful tracers for deconvolving physical from biogeochemical ocean variability on interannual to decadal timescales. But in order to decipher the variability signal, one first needs to remove the long-term CFC growth trends associated with the penetration of CFCs into the ocean interior. Several studies have used pCFC ages in this regard, keeping in mind the age bias issues raised above. For example, *Doney et al.* [1998a] compared CFC distributions along 20˚W in the eastern North Atlantic from transects in 1993 and 1988. They infer significant reductions in subpolar mode water convection and increases in saline, subtropical underwater between the two occupations. *Watanabe et al*. [2001] and *Mecking et al.* [2004a] infer a slowing in ocean circulation from the observed increase in pCFC ages (up to 4 years or 33-40%) and corresponding increases in apparent oxygen utilization (AOU) (up to 40 μmol/kg) in the eastern subpolar North Pacific from the mid 1980's/early 1990's to the late 1990's/2000. These pCFC age changes are significant, exceeding age error estimates, and persist even after corrections are made for the expected temporal mixing biases [*Mecking et al.,* 2004a]. The density surfaces in question (σ_θ=26.0 to 26.8 kg/m^3) outcrop in the central/western subpolar gyre, and several mechanisms could support the observed CFC signal including a northwestward shift in winter outcrops (lengthening of the ventilation path) to cessation of outcropping altogether.

A number of numerical simulations of CFC concentrations have been carried out to test the skill of global ocean general circulation models (OGCMs) [*England and Maier-Reimer*, 2001; *Dutay et al*., 2002; *Doney and Hecht*, 2002]. Some of these studies have considered seasonal variability of the surface forcing and resulting ocean circulation; others have employed steady state climatological oceanic conditions. The CFC simulation of *Craig et al*. [1998] considered inter-annually varying wind stress for the period 1976 to 1993 only and a repeating annual cycle of surface buoyancy forcing. *Thompson et al*. [2005] explore the effect of time-varying wind field on CFCs, oxygen, and ocean circulation in an isopycnal model for the North Pacific.

In this study, we simulate the evolution of CFC-11, CFC-12, and ideal age in a global OGCM using daily varying surface wind and buoyancy forcing based on NCEP /NCAR reanalysis data [*Kalnay et al.,* 1996]. With the aim of evaluating the usefulness of CFC data in determining variability in ventilation, we address the following questions: How do the simulated CFC concentrations and tracer ages compare to observations? How do the CFC based ages compare to one another and to ideal age and how do the differences between the age measures relate to those established with simpler models and the transit

time distributions (TTD) theory [*Hall et al.,* 2002]? Finally, what are the magnitude and pattern of inter-annual to decadal variability in CFC based and ideal age and how do they relate to changes in the physical circulation? While the simulation is global, we limit our analysis in this study to the subpolar/subtropical thermocline of the North Pacific due to the relatively good observational coverage for CFCs for that region [e.g., *Warner et al*., 1996] and the well documented decadal timescale variability of the circulation [*Miller et al., 2004*].

2. Methods

In this study we use the version of the Los Alamos Parallel Ocean Program (POP) developed for the NCAR Community Climate System Model (CCSM) version 2 [*Keihl and Gent*, 2004]. This configuration of POP includes the KPP vertical mixing scheme [*Large et al.,* 1994], the Gent-McWilliams eddy parameterization [*Gent and McWilliams*, 1990], and anisotropic horizontal viscosity [*Smith and McWilliams,* 2003]. The horizontal resolution is 1.125˚ in longitude and varies from 0.28˚ to 0.54˚ in latitude. There are 40 levels in the vertical with minimum spacing of 10m near the surface, increasing with depth to a maximum spacing of 250m. The surface turbulent fluxes of momentum, heat and freshwater were computed with bulk aerodynamic formulae using the model predicted sea surface temperature and the surface meteorological state (winds, air temperature, humidity) prescribed using NCEP/NCAR reanalysis data from 1958 to 2000 [*Doney et al.,* 1998b]. Satellite data products (clouds, insolation, precipitation) are used to prescribe the remaining surface fluxes. The procedures for specifying the surface forcing are described in detail by *Doney et al*. [2003]. The model is integrated for a total of 473 years by repeating this 43 year cycle of surface forcing 11 times.

The CFC-distributions are calculated during the last two cycles of the surface forcing. The prescribed atmospheric concentrations of CFC-11 and CFC-12 become nonzero beginning in 1945 (model year 1988 of cycle 10) and 1936 (model year 1979 of cycle 10), respectively. Air-sea gas exchange for the CFCs is specified as in the Ocean Carbon Cycle Model Inter-Comparison Project 2 (OCMIP2) [*Dutay et al.,* 2002]. A standard gas transfer formulation is used relating the flux to specified, time-evolving atmospheric partial pressure, the model surface CFC concentration, and a wind-speed derived gas transfer velocity. Figure 1 shows the reconstructed atmospheric concentration of CFC-11 and CFC-12 over time from *Walker et al*. [2000]. There was an error in this calculation, discussed in *Gent et al*. [submitted]. The transition between the northern and southern hemisphere atmospheric CFC partial pressure was imposed over +/- 10 radians instead of +/-10 degrees. The model hemispheric oceanic CFC inventories are biased by 5-10% (low in the Northern Hemisphere, high in the Southern Hemisphere) by the error. On the other hand, the error in the global oceanic CFC inventory is much smaller due to the compensation between the hemispheres (*Gent et al*., submitted). Equilibrium CFC partial pressures are computed to reduce the relatively large solubility affects on the CFC fields [*Doney and Bullister*, 1992]. The CFC-11 and 12 partial pressure age are computed by comparison to the prescribed atmospheric CFC forcing data [*Warner et al*., 1996]; the impact of the atmospheric CFC latitudinal error on the tracer ages is much smaller than on the simulated concentrations because the error is

accounted for in both the model forcing and age calculations. Ideal age, with a surface boundary condition of zero concentration and a uniform interior source of unit strength [*Thiele and Sarmiento*, 1990] is included from the beginning of the simulation.

3 Results

3.1 Comparison with Physical and CFC Observations

While the focus of this manuscript is on the temporal variability of tracers and age measures, we begin with a brief evaluation of the simulated physical circulation and its variability, with an emphasis on aspects related to subduction processes.

The winter (March) surface density and maximum mixed layer depth averaged over the last 43 year cycle of the forcing are shown in Figure 2a. Maximum winter mixed layer depths are found to the south of the Kuroshio Extension region, reaching 225 to 250m between 30˚N and 38˚N west of the dateline. While the maximum depths are comparable to observational estimates [e.g., *Ladd and Thompson*, 2000], the axis of deepest simulated mixed layer depths is displaced several degrees of latitude to the south of that in the observations. A second region of deep mixed layers is found in the eastern basin, centered on 140˚W, 27˚N and is the formation region for Eastern Subtropical Mode Water [*Ladd and Thompson*, 2000]. The simulated potential density in the upper ocean is compared with the WOA98 climatology [*Levitus et al*., 1998] along 165˚E in Figure 2b. The overall depth of the thermocline, as indicated by the depth of the σ_θ=27.0 isopycnal, is accurately simulated, but there are several notable discrepancies in the upper thermocline. First, the strong front associated with the Kuroshio Extension is displaced several degrees of latitude to the north of the observed position (e.g., note difference in position of σ_θ=26.0 isopycnal at ~39˚N). This is associated with the well known problem of poor western boundary current separation in coarse resolution models. Second, while a distinct pycnostad is apparent in the simulation, it occurs at too shallow of a density range. At this longitude, the simulated pycnostad is centered at ~30˚N and found between the σ_θ=25.0 and σ_θ=25.5 isopycnals, whereas it is located between the σ_θ=25.5 and σ_θ=25.75 isopycnals in the WOA98 climatology. Both the southward shift of the axis of deep winter mixed layers and the northward shift of the isopycnals in the western North Pacific lead toward the lighter densities in the simulated subducted subtropical mode water.

Lysne and Deser [2002] describe in detail the simulated interannual variability of the North Pacific and underlying physical mechanisms using the same surface forcing data and procedures but with a previous, coarser resolution, version of the CCSM ocean component [*Doney et al.,* 2003]. They find the simulation reproduces the observed patterns of thermocline variability reasonably well, with some exceptions noted below. The results from the present simulation are quite similar. For example, Figure 3 shows the mean and variance of annual average potential temperature at 200 m over the period 1968-1997 in the current simulation, for direct comparison with Figure 1 of *Lysne and Deser* [2002]. An approximately zonal band of elevated temperature variance is observed in the Kuroshio extension, associated with lagged (~4 years) changes in basin-scale wind stress curl. The simulated variance in this region is too low in the lower

thermocline and displaced several degrees northward. Maxima also occur along the equatorward flanks of the subtropical gyres in the Northern and Southern hemispheres. The *Lysne and Deser* [2002] analysis attributes this variability in about equal parts by changes in local Ekman pumping and westward propagating Rossby waves. The model variance along 10˚N is somewhat too large relative to observations.

Turning to the CFC simulation results, the time history of the global CFC inventory provides a zeroth order measure of the overall model behavior and skill. The global ocean CFC-11 inventory for the WOCE period (centered around 1994) was calculated by *Willey et al.* [2004] as $5.5(+/-1.2)x10^8$ moles. The simulated global inventory for the same time is $4.4x10^8$ moles, an underestimate of 20% and just inside the error bounds of the observations. This simulation also is at the lower end of the inventory estimates of the collection of models that participated in OCMIP-2 [*Dutay, et al*., 2002]. A slightly updated version of this model that is used as the ocean component in CCSM3 [*Gent et al., submitted*] produces a somewhat greater global CFC inventory, but remains at the low end of the estimate of *Willey et al.* [2004].

The CFC-11 inventory in the North Pacific, computed from the *Willey et al*. [2004] gridded analysis, is $6.9x10^7$ moles, while that computed from the simulated CFC-11 distribution is $5.3x10^7$ moles. The underestimate of 23% is thus somewhat greater than that for the global inventory. This may be attributed, in part, to the forcing error described above. Figure 4 shows the CFC-11 column inventory distribution in the North Pacific. A particularly notable discrepancy is the large underestimate in the western subtropical gyre. *Mecking et al.* [2004b] found a similar pattern of underestimated CFC concentration in this area (see figures 6 and 7 in *Mecking et al.* [2004b]) in their diagnostic model calculation when relatively low isopycnal eddy diffusivities were used. They obtained better fits to observations by locally increasing the isopycnal diffusivity to 5000 m^2s^{-1} in the region of the Kuroshio extension (from a background value of 2000 m^2s^{-1}). By comparison, the isopycnal eddy diffusion coefficient in our model has a spatially uniform value of 600 m^2s^{-1}, one order less than used by *Mecking et al.* [2004b].

Figure 5 shows a comparison of the observed and simulated meridional distributions of CFC-11 and potential density, and observed and simulated CFC column inventories along 165˚E in September 1992. The summer thermocline north of the Kuroshio extension is too strong and too shallow in the simulation. As was the case in the climatology described in Figure 2, the pycnostad associated with subtropical mode water (STMW) occurs higher in the water column and at a lighter density, in the range σ_θ=25.0 to 25.5 in the model compared with σ_θ=25.5 to σ_θ=26.0 in the observed section. CFC-11 penetrates furthest into the subtropical gyre at the top of the STMW, and in consequence is at too light of a density and too shallow of a depth in the simulation. The penetration of CFCs is especially weak near 40˚N, the “mixed-water region” [*Qu et al., 2001*] between the Kuroshio and Oyashio fronts. The model produces only a single front and is unable to simulate the dynamical complexity of the region. In the observations, the penetration of CFC-11 at a concentration of 1.0 pmol kg^{-1} occurs at a potential density of approximately σ_θ=27.0. On the other hand, the simulated penetration is shallower and does not correspond as closely to the base of the

thermocline. The low biases in the simulated subsurface CFC distributions and water-column inventories extend beyond the 165˚E section and occur across much of the basin.

Figure 6 shows a comparison of the observed and simulated zonal distributions of CFC-11 and potential density, and observed and simulated column inventories along 24˚N in April 1985. The observed CFC-11 penetration is shallower in the east and deeper in the west. The simulated depth of penetration is in good agreement with observations in the east, but is too zonally uniform, resulting in an underestimate in the west. The surface concentration is higher in the east and lower in the west, mostly due to thermal solubility effects, with the model in good agreement with observations. The simulated column inventory is up to a factor of 2 times lower than observed.

The model errors cannot simply be explained by temperature biases in the simulation (recall that CFC solubility decreases sharply with temperature) because the simulated thermocline pCFC ages are also overestimated in the model (see below). Thus the CFC biases must reflect overly weak thermocline ventilation in the simulation. In OCMIP-2, a similar underestimation of ventilation in the middle latitudes of the North Pacific was found in all the models [*Dutay et al.*, 2002]. The biases in the simulated density structure and mixed layer depths described above, and their impact on subduction of subtropical mode water, present a hypothesis for the cause of the model CFC deficiencies. The biases in the CFC simulation somewhat complicate comparisons to data or the direct application of the model age fields to geochemical problems; but the errors do not detract fundamentally from the internal model tracer-tracer and tracer-ideal age comparisons detailed below. The impact of the ventilation errors on the model generated tracer and age inter-annual variability are not completely understood, however, and the simulated variability fields should be considered illustrative of the patterns and magnitudes.

As a first examination of the temporal variability of CFCs in the model, Figure 7(a) shows the temporal changes of the CFC profile versus potential density at 24˚N, 140˚W for direct comparison with Figure 13 of *Mecking and Warner* [2001]. As observed, the potential density of the simulated CFC maximum increases over time by approximately 1.0 kg m^{-3}, but with an overall offset of 0.5 toward lighter density compared to observations. *Mecking and Warner* [2001] attribute the descent of the CFC maximum to change in the atmospheric CFC growth rate and provide a simple expression for the vertical dependence of the CFC maximum (their equation 4). We test the equation using model simulated solubility and pCFC-12 age profiles from three different dates. The very simple equation captures the density change in the simulated CFC maximum, but the timing of the descent is dependent on the choice of dates used for the solubility and age. In particular, using age profiles estimated after 1995 results in an unrealistic delay in the beginning of the descent of the CFC maximum. Figure 7(b) shows the temporal changes of the simulated CFC profile versus at 24.9˚N, 165.4˚E. This point is near the crossover of the meridional and zonal sections shown in Figures 5 and 6. At this site, the simple diagnostic again predicts a similar vertical descent as was actually simulated by the full model and again the timing is dependent on the date used for the reference solubility and age. *Mecking and Warner* [2001] tabulate the potential density of the

CFC-11 and CFC-12 maxima at the crossover of selected cruises in the North Pacific. At this location in 1992, the observed potential densities of the CFC-11 and CFC-12 maxima are at 25.45 and 25.40, respectively. The simulated potential densities of CFC-11 and CFC-12 maximum are 25.2 and 25.3, respectively for the same year. In summary, while there is a systematic bias towards shallow penetration of CFCs in the simulation, the secular trends in the vertical distribution of CFCs are well captured by the model.

3.2 CFC ages and ideal age

In the following, we focus on the pCFC-12 age because it is well defined through most of the integration period, allowing an examination of variability in the later part of the run. Figure 8 shows the meridional distribution of observed pCFC-12 age and model pCFC-12 and ideal age along 165°E in 1992. The simulated pCFC-12 ages are significantly older than observed for σ_θ greater than approximately 26.0 because the calculated CFC-12 penetration below this isopycnal is too low. Above this isopycnal, the agreement is relatively good though still not perfect. In contrast to the CFC concentration, there is no local extremum in age associated with the subducted mode water in either the model or the observations. Figure 9 shows the zonal distribution of observed pCFC-12 age and model pCFC-12 and ideal age along 24°N in 1985. The simulated pCFC-12 age is in relatively good agreement with observations, but is substantially younger than ideal age. The pCFC-12 age distributions do not capture the very large vertical age gradient centered on 200m that is apparent in the ideal age distribution, resulting in increasing bias with increasing age.

Figure 10 shows the scatter plot of the ratio pCFC-12 age/ideal age vs pCFC-12 age along WOCE section P13 at 165˚E in 1992 from the simulation. The ratio of pCFC-12 age and ideal age converges to 0.15 for pCFC-12 age in excess of 25 years. For pCFC-12 ages between 1 and 5 years, the ratio can exceed 1. The overestimate of pCFC-12 age relative to ideal age may be caused by under-saturation of surface waters. When pCFC age is calculated from CFC concentrations, temperature, and salinity and the atmospheric time history, 100% saturation at the time of subduction is assumed. Therefore, under-saturation of CFC may lead to an overestimate of pCFC age, possibly exceeding ideal age. In addition, change in the curvature of the CFC time history in the later period may lead to an overestimate of pCFC age.

Figure 11 shows the distribution of simulated pCFC-12 age, ideal age and the ratio of pCFC-12 age/ideal age on the σ_θ=25.4 isopycnal in 1992. The ratio is almost 1 around the outcrop area and remains closest to 1 along a tongue of directly ventilated circulation that reaches the western boundary near 20°N. The ratio is small (<0.3) along the southern flank of the subtropical gyre. *Mecking et al*. [2004b], using a two-dimensional advection-diffusion model on isopycnal surfaces, found much smaller differences between pCFC-12 and ideal age in this region. In their case however, the boundary condition along 10˚N (the southern boundary of their model) constrained the pCFC-12 age and ideal age to be the same. We see here that the differences are maximized along this latitude.

3.3 Temporal variability of age measures

Spatial maps of the root-mean-square (rms) variability of monthly means of ideal age and potential vorticity (PV) on σ_θ=25.4 over the last model forcing cycle are shown in Figure 12. The outcrop mask shown in these figures is the maximum area; i.e., the area is masked out where the outcrop occurred at least once in the 43 years x 12 monthly means. The variability of ideal age is large along 15˚N where there is a strong front in age at the edge of the ventilated zone. The variability is largest near 150˚W where the meridional gradient of age is strongest. The spatial and temporal variability of PV is similar to that of CFC in some respects. There is a local maxima in the variability of PV in the same area as for ideal age. The meridional gradient of PV diminishes much more rapidly in the western basin than does that of age, so the rms maxima in PV does not extend as far to the west. Note that by averaging on isopycnal surfaces, any heaving effect of isopycnal displacements is removed, so the large variability indicated in Figure 12 is a signature of meridional displacements in the position of the age and PV fronts along the edge of the shadow zone of the subtropical gyre. This is the tracer signature of the propagation of Rossby waves described by *Lysne and Deser* [2002].

The spatial distribution of rms variability of monthly means of ideal age and PV on the σ_θ=26 isopycnal over the last model forcing cycle is shown in Figure 13. On this surface, the variability in both ideal age and PV become more prominent near the outcrop, though in both Figure 12 and 13 interannual PV variability extends further east along the outcrop, and less pronounced along the southern flank of the gyre. The variability along 13˚N has a dominantly first baroclinic mode structure [*Lysne and Deser*, 2002], with the maximum energy located above the mean depth of the σ_θ=26 surface. Additionally, the contrast in age across the front decreases on deeper surfaces.

The nature of the ideal age variability summarized in the statistical measures described above is illustrated with two snapshots of the σ_θ=25.4 surface in March 1969 and March 1986 in Figure 14. In addition to the distribution of ideal age, we show the region of deepest mixed layers (> 150 m) and the Montgomery potential, the streamlines for the geostrophic flow:

$$M = p(z_\sigma) - gz_\sigma \rho(z_\sigma)$$

where p is the pressure, z_σ is the depth of the isopycnal surface, g is the gravitational acceleration, and ρ is the in situ density. These two years span the shift during the mid-1970's of the "Pacific Decadal Oscillation" (PDO), a long-lived pattern of Pacific climate variability [*Mantua and Hare*, 2002]. The atmospheric patterns associated with the PDO include a strengthening and southward shift of the Aleutian low, with the ocean responding with a strengthening of the subtropical and subpolar gyres [*Suga et al*., 2000; *Schneider et al*., 2002], a strengthening and southward shift of the Kuroshio [*Yasuda and Hanawa*, 1997; *Deser et al*., 1999; *Tatebe and Yasuda,* 2005], increased heat loss and deepening of maximum winter mixed layer depths in the central and western Pacific [*Chai et al*., 2003], and an eastward displacement of the location for subduction of subtropical mode waters [*Xie et al.,* 2000]. Each of these features can be seen in Figure 14. The strengthening of the circulation after the mid-1970's is indicated by the tighter spacing of streamlines, and the eastward flow of the Kuroshio becomes

visible at lower latitude. The region of deep mixed layers extends further to the east and south. The main location for subduction on the isopycnal is located at the intersection of the outcrop and the zone separating deep from shallower mixed layers. A broad decrease in age within the ventilated zone is apparent for the later year. Further details of the impact of these changes in the circulation on ideal age are discussed for selected sections below.

The variability of ideal age along 165˚E on the σ_θ=25.4 and σ_θ=26.0 surfaces is shown in Figure 15. Recalling that the atmospheric forcing is applied periodically for 1958-2000, we disregard variability in the first several years. A transition from higher to lower ages is seen near the outcrop of the σ_θ=25.4 surface around 1969. At this time the edge of the region of deep mixed-layers (Figure 2a) contracts toward the west and the isopycnal outcrop moves south between 160˚E and the dateline (Figure 14a). The result is that the location of mode water subduction migrates to the west, closer to the 165˚E section. The area of recirculating water south of the Kuroshio also retracts to the west, resulting in a sharp decrease in age as the boundary between the ventilated zone and the recirculation (also referred to as the western shadow zone) crosses the section. Beginning in the mid-1970's and through the 1980's (Figure 14b) the Kuroshio Extension axis shifts to the south and increases in transport. The location of mode-water subduction shifts back to the east, and the increased advection of older water from the western boundary just south of the outcrop results in increasing ages between 30˚N and 35˚N. The increasing strength of the westward flow of the subtropical gyre in the late 1970's results in enhanced penetration of the tongue of low age water to the west near 25˚N. A southward shift of the outcrop during 1995-1997 results in a decrease in age, similar to the 1970's, with more direct ventilation near the 165˚E section.

The largest amplitude variability on the 165˚E section occurs along the age front to the south of the directly ventilated zone near 13˚N. Both decadal timescale variations of the position of the front and annual timescale variations, with a tendency for northward excursions of the front (positive age anomalies) at the beginning of the calendar year, and southward excursions (negative age anomalies) in mid-year, are apparent. The variations on both timescales on the σ_θ=26 surface at this latitude (Figure 15b) are in phase with those above but with slightly reduced amplitude.

The σ_θ=26.0 isopycnal outcrops north of the region of deep winter mixed layers in the simulation, and the main region of subduction for this surface is east of the dateline between 40˚N and 45˚N. The ages along 35˚N tend to be anti-correlated with those on σ_θ=25.4. In contrast, the variations of age within the ventilated zone of westward flow tend to be directly correlated with those on the lighter surface, with decreasing ages as the subtropical gyre strengthens following the PDO shift of the mid-1970's.

Looking further to the west, at 150˚E (Figure 16a), we also see the signature of decreasing ages in the ventilated zone following the PDO shift. Closer to the outcrop, (30˚N to 35˚N), the water is more directly influenced by the Kuroshio. The age of Kuroshio water tends to be older in the early part of the run (Figure 14a). As the transport of the subtropical gyre increases, the lower age water of the directly ventilated zone is eventually incorporated into the western boundary current, leading to a decline

in the age of the Kuroshio waters, and this is reflected in decreasing age to the south of the outcrop through the 1980's.

At 152˚W (Figure 16b), the ages are generally much younger and the outcrop latitude more variable. Anomalies in age tend to be more directly related to shifts in the outcrop position. Notable southward excursions of the outcrop and eastward expansion of the region of deep mixed layers, with consequent decreases in age, occur in 1983 and 1998 associated with strong ENSO events. A second source of ventilation of this isopycnal occurs through Eastern Subtropical Mode Water (ESTMW) just to the east of this section. The σ_θ=25.4 isopycnal does not outcrop in the ESTMW region, but is influenced through mixing from above. This variety of mode water was weakly ventilated in the late 1970's, resulting in an increase in age between 20˚N and 25˚N. The variability of age along the front near 13˚N is stronger here than on the sections to the west. The westward propagation of individual disturbances is also apparent by comparing the three sections (disturbances arriving successively later in figures 16b, 15a and 16a).

We now turn to the relationship between the variability of CFC concentrations, pCFC ages and PV and that of ideal age by examining timeseries of each variable on the σ_θ=25.4 surface at three locations representative of different flow regimes within the subtropical gyre. The first point we examine is at 20˚N, 165˚E, within the westward flowing tongue of directly ventilated water (Figure 17a). As indicated above, the age in this region increases until the mid-1970's then declines with the increasing strength of the subtropical gyre. A long-term trend of increasing pCFC ages through time is apparent with an initial offset from ideal age of 5 to 6 years, approaching zero by the end of the integration. This change can be attributed to pCFC age biases resulting from mixing and the nonlinear time history of the atmospheric history of CFCs [*Waugh et al.,* 2003]. The inter-annual to decadal timescale variability of pCFC ages is coherent with that in ideal age, but with reduced amplitude. The variability in PV is relatively small (+/- 10%) within the core of the directly ventilated water, and has a less obvious relationship to variations ideal age.

The next point considered is at 30˚N, 150˚W, close to the outcrop of the σ_θ=25.4 isopycnal where the ages are very young (Figure 17b). The sharp decrease in age following the 1983 and 1997 ENSO events mentioned above is apparent in these timeseries. Even though the offset between ideal age and pCFC ages is relatively small, the amplitude of the inter-annual to decadal variability of pCFC ages still underestimates that of ideal age. At this location, there is an association between PV and age for some, but not all events.

The final location we examine is at 15˚N, 150˚W, in the region of strong age variability at the front between the ventilated and shadow zones (Figure 17c). Here the mean ideal age approaches the length of the atmospheric CFC transient, pCFC ages underestimate the ideal age by a factor of 5-10, and the increase in pCFC age through time is readily apparent. The rms variability of pCFC ages is a small fraction of that of ideal age. There is a very strong correlation between variability of PV and age at this location. We discuss the variability at this location in more detail below. *Min et al.,* [2000] have

identified non-monotonic trends in observed CFC-11 concentration from repeat measurements near 30°N, 122°W. It is difficult to compare their observations close to coast with our simulation due to the resolution of our model, but their repeat station is near the boundary of the shadow zone where we have found large inter-annual variability.

4. Discussion and Conclusions

Our results confirm that pCFC ages underestimate ideal age and have a generally increasing trend through time as a result of nonlinear mixing effects as described in numerous previous studies [e.g. *Sonnerup,* 2001, *Waugh et al.,* 2003, *Mecking et al.*, 2004b]. We find larger ratios of ideal age to pCFC age than found in previous studies particularly in the southern and deeper parts of the gyre; this can be largely attributed to the artificial open boundary condition imposed in the idealized [*Sonnerup*, 2001] or regional [*Mecking and Warner*, 2001] models used in earlier studies.

While at all points examined the variability in pCFC ages is coherent with that of ideal age, it is reduced in amplitude. This result is especially obvious at some points (such as illustrated in Figure 17c) where the peak-to-peak variations in ideal age exceed the time mean pCFC age. Removing the trend in pCFC ages due to nonlinear mixing effects, as done for example by *Mecking, et al.* [2004a], is a necessary but not a sufficient correction to estimate changes in ventilation from CFC based ages. The reduced amplitude of the pCFC age variability must also be taken into account.

We have seen from the simulations that a number of processes can contribute to changes in age measures. Broadly speaking, we can distinguish between those that result from changes in the rate of subduction or distance from the outcrop and those resulting from wave-like spatial displacements of water masses that conserve their properties. For the latter we would expect the perturbations in age at a point to be proportional to the local mean gradient of age, i.e.,

$$\tau' = L' \bullet \nabla \bar{\tau}$$

where L' is the displacement vector for a water parcel and the gradient is evaluated along an isopycnal. The ratio of ideal age to pCFC age variations should then be proportional to the ratio of their time mean spatial gradients. We illustrate this relationship at the point shown in Figure 17c where the age changes are clearly associated with frontal displacements and the gradient is closely aligned with the meridional direction. Without an independent estimate of the long-term changes in pCFC age due to the nonlinear mixing effect, we use a quadratic fit to define the slowly evolving "mean" about which the perturbations occur, and remove the 43 year mean from ideal age to obtain the ideal age perturbations (Figure 18a). An estimate of the ratio of the mean gradients is obtained from the merdional slope of the quadratic fit to pCFC age and the mean ideal age between 10˚N and 15˚N averaged over a 10˚ zonal band centered on 150˚W. In Figure 18b we show two adjusted estimates of pCFC ages: one rescaled by the ratio of the mean ideal age to the long term pCFC fit, $\bar{\tau}_{ideal} / \bar{\tau}_{pCFC12}$, and one rescaled by the ratio of their meridional gradients. The relative success of the three pCFC based age measures in matching the ideal age is summarized in Table 1. It is clear that the ratio of pCFC age perturbation amplitude to ideal age perturbation

amplitude is more closely associated with the relative magnitudes of the gradients in these fields than in the ratio of the local ages themselves. In other words, considering the age variations in terms of percentage change from the time mean still does not explain the difference in the amplitude of changes in ideal age and pCFC age. This example was particularly simple because the displacement vector and mean age gradient are nearly parallel and happen to be in the direction along the section. In the more general case it would be difficult to interpret changes between repeat sections because knowledge of both the mean spatial gradients and parcel displacements in directions outside the section would be required.

The strong relationship between PV and age in this setting is also clear since PV perturbations will follow a similar relationship to the mean PV gradients for wave-like disturbances. Within the ventilated zone (e.g. Figure 17b) we cannot expect such a close relationship. The PV of the subducted water can be changed not only by the subduction rate, but also spacing of isopycnals and slope of the base of the mixed layer in the direction of the flow at the location of subduction (*Williams*, 1991). In contrast the age of the subducted water will always be zero, irrespective of the geometry of subduction.

The sparsity of CFC observations in time makes it difficult to interpret changes between two surveys. The simulation presented here illustrates substantial inter-annual to decadal timescale variability of ages at many locations around the gyre. The sparse sampling of this variability could lead to serious aliasing problems when trying to deduce trends in ventilation from repeat occupations spaced 5 or more years apart. This difficulty is compounded by the biases between pCFC ages and ideal age. Long-term trends in CFC based ages tend to lead to an over estimate of the change in ventilation. Attempts have been made to compensate for this effect with an additive correction [e.g., *Mecking* et al., 2004a; *Bullister et al.,* 2004]. Our results show that this is necessary, but not sufficient in at least some circumstances. An additional multiplicative correction is necessary to account for biases in the spatial gradients of CFC based ages as well. Ultimately, a comprehensive data assimilation system for tracers based on ocean general circulation models forced with observed atmospheric conditions may aid in placing these changes into the full dynamical context and provide quantitative estimates of ocean ventilation and its variability across all time scales.

Acknowledgement
We thank Y. Yoshida, K. Lindsay, S. Yeager, N. Nakashiki for their contributions to the model integration. We also thank J. Bullister for providing us with access to the WOCE North Pacific CFC observation and all of the members WOCE CFC science team for their dedication and hard work. The National Center for Atmospheric Research is sponsored by the U.S. National Science Foundation. M. Hecht was supported by the Climate Change Prediction Program in the U.S. Department of Energy's Office of Science. This is Woods Hole Oceanographic Institution contribution # XXXXX and Los Alamos Unlimited Release # XXXXX.

References

Bullister, J.L. (1989), Chlorofluorocarbons as time-dependent tracers in the ocean, *Oceanography, 2,* 12-17.

Bullister, J.L., M.J. arner, R.E. Sonnerup, G.C. Johnson, and N. Gruber (2004), Decadal changes in dissolved CFCs in the eastern basin of the North Atlantic, *Eos Trans. AGU, 85, Fall Meeting Suppl.*

Chai, F., M. Jiang, R. T. Barber, R. C. Dugdale, andY. Chao (2003), Interdecadal Variation of the Transition Zone Chlorophyll Front: A Physical-Biological Model Simulation between 1960 and 1990, *J. Oceanogr., 59,* 461-475.

Craig, A.P., J.L. Bullister, D.E. Harrison, R.M. Chervin and A.J. Semtner Jr. (1998), A comparison of temperature, salinity and chlorofluorocarbon observations with results from a 1˚ resolution three-dimensional global ocean model, *J. Geophys. Res., 103*(C1)*,* 1099-1119.

Deser, C., M.A. Alexander and M. Timin (1999), Evidence for a wind-driven intensification of the Kuroshio Current Extension for the 1970s to the 1980s, *J. Climate*, *12,* 1697-1706.

Doney, S.C. and J.L. Bullister (1992), A chlorofluorocarbon section in the eastern North Atlantic, *Deep Sea Res. I*, *39,* 1957-1881.

Doney, S.C., J.L. Bullister, and R. Wanninkhof (1998a), Climatic variability in upper ocean ventilation diagnosed using chlorofluorocarbons, *Geophys. Res. Lett.*, *25,* 1399-1402.

Doney, S.C. and M.W. Hecht (2002), Antarctic Bottom Water Formation and deep water chlorofluorocarbon distributions in a global ocean climate model, *J. Phys. Oceanogr.*, *32,* 1642-1666.

Doney, S.C., W.J. Jenkins, and J.L. Bullister (1997), A comparison of ocean tracer dating techniques on a meridional section in the eastern North Atlantic, *Deep-Sea Res. I*, *44,* 603-626.

Doney, S.C., W.G. Large, and F.O. Bryan (1998b), Surface ocean fluxes and water-mass transformation rates in the coupled NCAR Climate System Model, *J. Climate*, *11,* 1422-1443.

Doney, S.C., S. Yeager, G. Danabasoglu, W.G. Large, and J.C. McWilliams (2003), Modeling oceanic interannual variability (1958-1997): Simulation design and model-data evaluation, *NCAR Technical Report*, NCAR/TN-452+STR, 48pp.

Dutay, J.-C., J.L. Bullister, S.C. Doney, J.C. Orr, R. Najjar, K. Caldeira, J.-M. Champin, H. Drange, M. Follows, Y. Gao, N. Gruber, M.W. Hecht, A. Ishida, F. Joos, K. Lindsay, G. Madec, E. Maier-Reimer, J.C. Marshall, R.J. Matear, P. Monfray, G.-K. Plattner, J. Sarmiento, R. Schlitzer, R. Slater, I.J. Totterdell, M.-F. Weirig, Y. Yamanaka, and A.

Yool (2002), Evaluation of ocean model ventilation with CFC-11: comparison of 13 global ocean models, *Ocean Modelling*, *4,* 89-120.

England,M. H. (1995), The Age of Water and Ventilation Timescales in a Global Ocean Model, *J. Phys. Oceanogr.*, *25,* 2756-2777.

England, M.H., and E. Maier-Reimer (2001), Using chemical tracers to assess ocean models, *Rev. Geophys.*, *39* (1), 29-70.

Gent, P.R. and J.C. McWilliams (1990), Isopycnal mixing in ocean circulation models, *J. Phys. Oceanogr.*, *20,* 150-155.

Gent, P. R., F. O. Bryan, G. Danabasoglu, K. Lindsay, D. Tsumune, M. W. Hecht, S. C. Doney, Ocean Chlorofluorocarbon and Heat Uptake During the 20th Century in the CCSM3, *J. Climate*, submitted.

Gruber, N., J.L. Sarmiento, and T.F. Stocker (1996), An improved method for detecting anthropogenic CO_2 in the oceans, *Global Biogeochem. Cycles*, *10,* 809-837.

Haine, T.W.N. and T.M. Hall (2002), A generalized transport theory: water-mass composition and age, *J. Phys. Oceanogr.*, *32,* 1932-1946.

Hall, T. M., T. W. N. Haine, and D. W. Waugh (2002), Inferring the concentration of anthropogenic carbon in the ocean from tracers, *Global Biogeochem. Cycles*, *16*(4), 1131, doi:10.1029/2001GB001835.

Holzer, M. and T.M. Hall (2000), Transit-time and tracer-age distributions in geophysical flows, *J. Atmos. Sci.*, 57, 3539-3558.

Kalnay, E., M. Kanamitsu, R. Kistler, W. Collins, D. Deaven, L. Gandin, M. Iredell, S. Saha, G. White, J. Woollen, Y. Zhu, M. Chelliah, W. Ebisuzaki, W. Higgins, J. Janowiak, K.C. Mo, C. Ropelewski, A. Leetmaa, R. Reynolds, and R. Jenne (1996), The NCEP/NCAR reanalysis project, *Bull. Amer. Meteor. Soc., 77,* 437-471.

Kiehl, J. T., and, P. R. Gent (2004), The Community Climate System Model, Version 2, *J. Climate*, *17,* 3666-3682.

Ladd, C. and L. Thompson (2000), Formation mechanisms for North Pacific central and eastern subtropical mode waters, *J. Phys. Oceanogr.*, *30,* 868-887.

Large, W.G., J. C. McWilliams, and S. C. Doney (1994), Ocean vertical mixing: A review and a model with a nonlocal boundary layer parameterization, *Rev. Geophys.*, *32,* 363-403.

Large, W.G., G. Danabasoglu, S.C. Doney, and J.C. McWilliams (1997), Sensitivity to surface forcing and boundary layer mixing in a global ocean model: annual-mean climatology, *J. Phys. Oceanogr.*, *27,* 2418-2447.

Levitus, S., T. Boyer, M. Conkright, D. Johnson, T. O'Brien, J. Antonov, C. Stephens, and R. Gelfeld (1998), World Ocean Database 1998, Volume 1: Introduction. NOAA Atlas NESDIS 18, U.S. Government Printing Office, Wash., D.C., 346 pp.

Lysne, J. and C. Deser (2002), Wind-driven thermocline variability in the Pacific: A model-data comparison, *J. Climate*, *15,* 829-845.

Mantua, N. J. and S. R. Hare (2002), The Pacific Decadal Oscillation, *J. Oceanography*, *58,* 35-44.

Mecking, S. and M.J. Warner (2001), On the subsurface CFC maxima in the subtropical North Pacific thermocline and their relation to mode waters and oxygen maxima, *J. Geophys. Res.*, *106,* 22,179-22,198.

Mecking, S., M.J. Warner, and J.L. Bullister (2004a), Age and AOU increases at the North Pacific subtropical-subpolar gyre boundary, *Deep-Sea Res. I*, submitted.

Mecking, S., M.J. Warner, C.E. Greene, S.L. Hautala, and R.E. Sonnerup (2004b), The influence of mixing on CFC uptake and CFC ages in the North Pacific thermocline, *J. Geophys. Res.*, *109,* C07014, doi:10.1029/2003JC001988.

Miller, A.J., F. Chai, S. Chiba, J.R. Moisan, and D.J. Neilson (2004), Decade-scale climate and ecosystem interactions in the North Pacific Ocean, *J. Oceanography*, *60,* 163-188.

Min, D., J. L. Bullister, and R. F. Weiss (2002), Anomalous chlorofluorocarbons in the Southern California Borderland Basins, *Geophys. Res. Lett.*, *29,* 1955, doi:10.1029/2002GL015408.

Qu, T., H. Mitsudera, and B. Qiu (2001), A Climatological View of the Kuroshio/Oyashio System East of Japan, *J. Phys. Oceangr.*, *31,* 2575-2589.

Schneider, N., A. J. Miller, and D. W. Pierce (2002), Anatomy of North Pacific Decadal Variability, *J. Climate*, *15*, 586–605.

Smith, R.D. and J.C. McWilliams (2003), Anisotropic horizontal viscosity for ocean models, *Ocean Modelling, 5,* 12-156.

Sonnerup, R.E. (2001), On the relation between CFC derived water mass ages, *Geophys. Res. Lett.*, *28,* 1739-1742.

Sonnerup, R.E., P.D. Quay, and J.L. Bullister (1999), Thermocline ventilation and oxygen utilization rates in the subtropical North Pacific based on CFC distributions during WOCE, *Deep-Sea Res. I, 46,* 777-805.

Suga, T., A. Kato, and K. Hanawa (2000), North Pacific Tropical Water: Its climatology

and temporal changes associated with the regime shift in the 1970s, *Prog. Oceanogr., 47,* 223-256.

Tatebe, H. and I. Yasuda (2005), Interdecadal variations of the coastal Oyashio from the 1970s to the early 1990s, *Geophys. Res. Letters, 32,* L10613, doi:10.1029/2005GL022605.

Thiele, G. and J.L. Sarmiento (1990), Tracer dating and ocean ventilation, *J. Geophys. Res., 95,* 9377-9391.

Thompson, L., I.D. Lima, S. Emerson, and C. Deutsch (2005), Changes in apparent oxygen utilization in the North Pacific: physical or biological causes?, *Global Biogeochem. Cycles*, in prep.

Walker, S.J., R.F. Weiss, and P.K. Salameh (2000), Reconstructed histories of the annual mean atmospheric mole fractions for the halocarbons CFC-11, CFC-12, CFC-113, and carbon tetrachloride, *J. Geophys. Res., 105,* 14,285-14,296.

Warner, M.J., J.L. Bullister, D.P. Wisegarver, R.H. Gammon, and R.F. Weiss (1996), Basin-wide distributions of chlorofluorocarbons CFC-11 and CFC-12 in the North Pacific: 1985-1989, *J. Geophys. Res., 101,* 20,525-20,542.

Warner, M.J. and R.F. Weiss (1985), Solubilities of chlorofluorocarbons 11 and 12 in water and seawater, *Deep-Sea Res. A*, *32,* 1485-1497.

Watanabe, Y.W., T. Ono, A. Shimamoto, T. Sugimoto, M. Wakita, and S. Watanabe (2001), Probability of a reduction in the formation rate of the subsurface water in the North Pacific during the 1980s and 1990s, *Geophys. Res. Lett., 28,* 3289-3292.

Waugh, D.W., T.M. Hall, and T.W.N. Haine (2003), Relationships among tracer ages, *J. Geophys. Res., 108*(5), doi:10.1029/2002JC001325.

Willey, D.A., R.A. Fine, R.E. Sonnerup, J.L. Bullister, W.M. Smethie, M.J. Warner (2004), Global oceanic chlorofluorocarbon inventory, *Geophys. Res. Lett., 31,* L01303, doi:10.1029/2003GL018816, 2004.

Williams, R.G. (1991), The role of the mixed layer in setting the potential vorticity of the main thermocline, *J. Phys. Oceanogr.*, *21,* 1803-1814.

Xie, S.-P., T. Kunitani, A. Kubokawa, M. Monaka, and S. Hosoda (2000), Interdecadal thermocline variability in the North Pacific for 1958-97: A GCM simulation, *J. Phys. Oceanogr.*, *30,* 2798-2813.

Yasuda, T., and K. Hanawa (1997), Decadal changes in the mode waters in the midlatitude North Pacific, *J. Phys. Oceanogr.*, *27,* 858-870.

Table 1. Standard deviation, Ratio to Standard deviation of ideal age, and regression coefficient with ideal age for ideal age, pCFC age, adjusted pCFC ages.

	Ideal Age	pCFC Age	pCFC Age adjusted by ratio of means	pCFC age adjusted by ratio of mean gradients
Std. Deviation	13.2	1.4	4.8	9.4
Ratio to Std.Deviation of Ideal Age	1.0	0.11	0.37	0.71
Regression Coeff. With ideal age	1.0	0.08 (0.003)	0.29 (0.010)	0.58 (0.018)

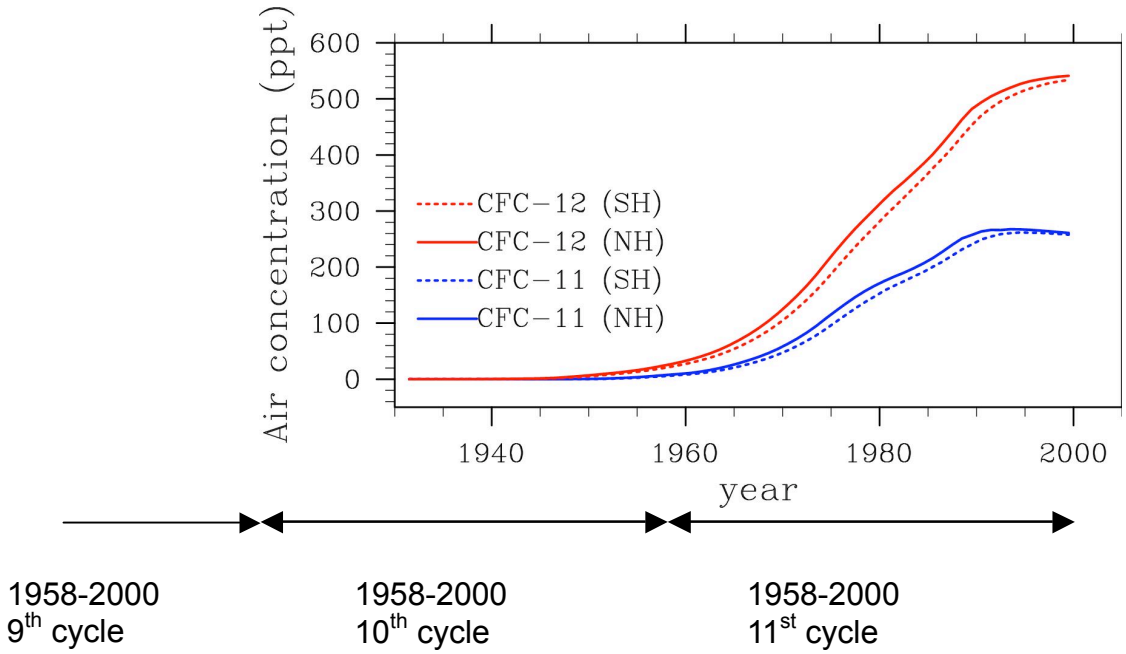

Figure 1. Time histories of the global mean atmospheric CFC-11 (blue) and CFC-12 (red) mole fractions (ppt) [*Walker et al.,* 2000]. Also shown is the relationship of the atmospheric CFC simulation to the repeating 43-year historical forcing cycle used to drive the ocean physical simulation.

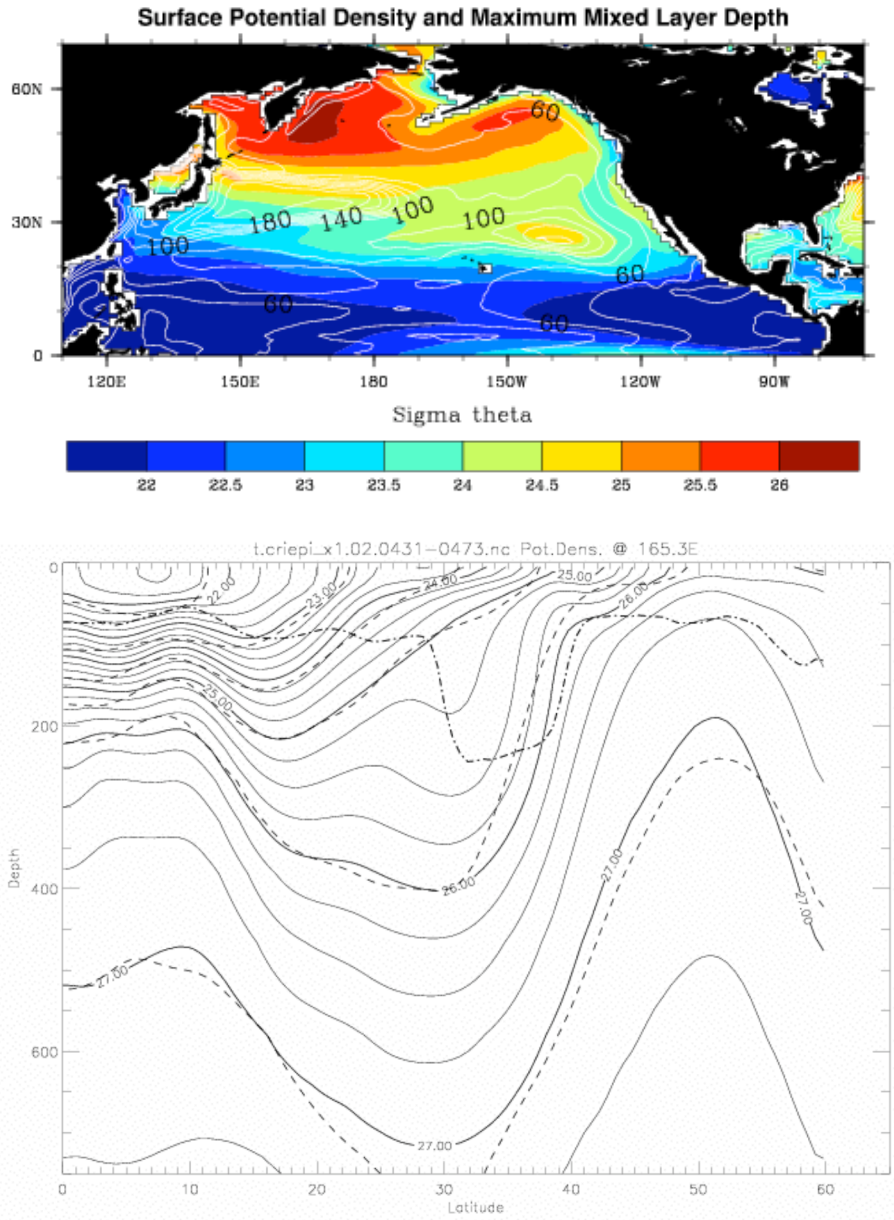

Figure 2. a) Simulated March surface density (color contours) and maximum mixed layer depth (white line contours) averaged over the period 1958-2000. b) Annual average potential density along 165˚E from the simulation (solid contours, interval = 0.25 kg m^{-3}), WOA98 [*Levitus et al*., 1998] (dashed contours, interval = 1.0 kg m^{-3}), and simulated maximum March mixed layer depth (dash-dot curve).

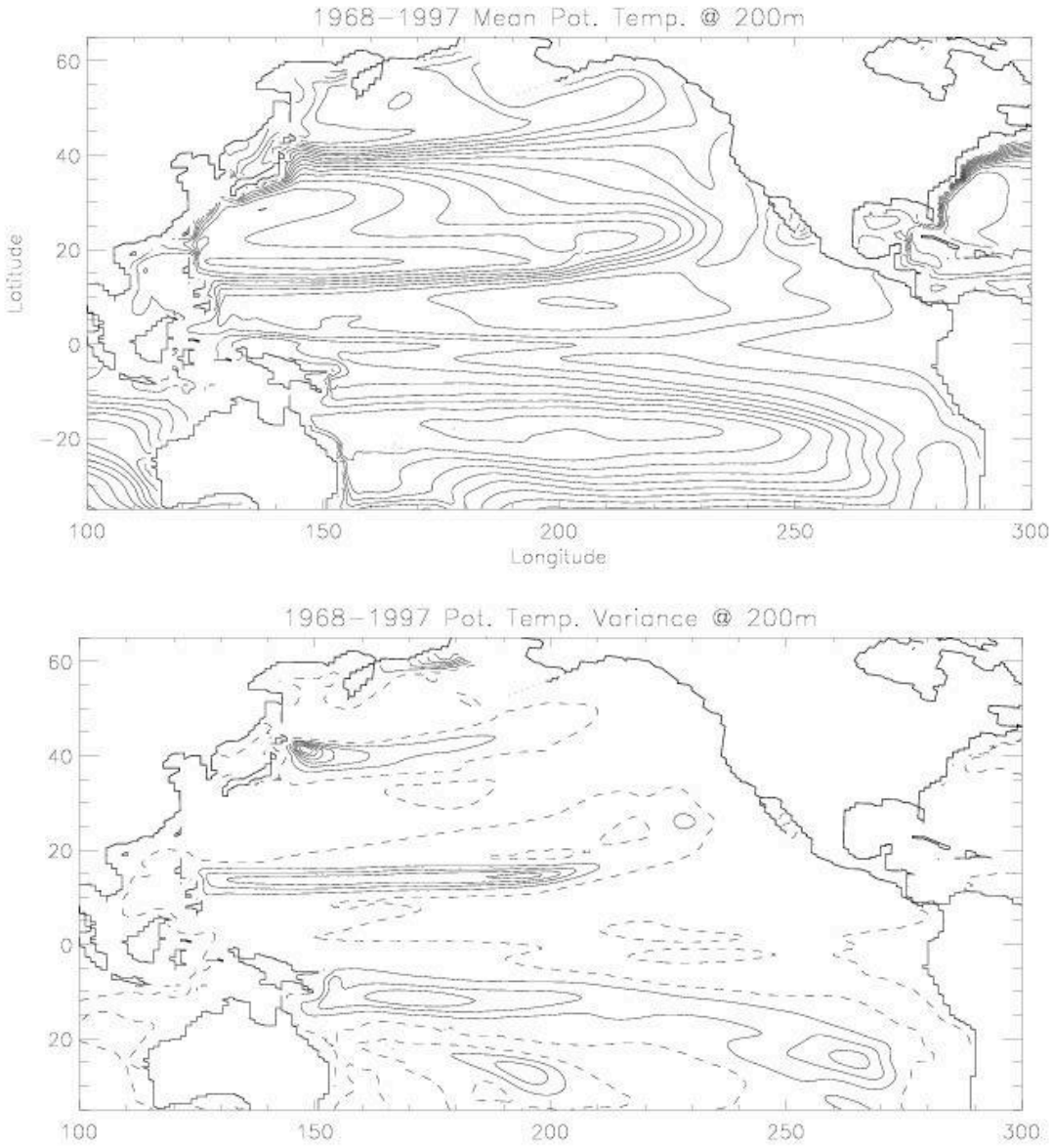

Figure 3. Mean distribution a) and interannual variance of simulated potential temperature field at 200 m. Dashed contour is at 0.1 K^2, solid contours are at an interval of 0.2 K^2. For the comparison with Figure 1 in *Lysne and Deser* [2002].

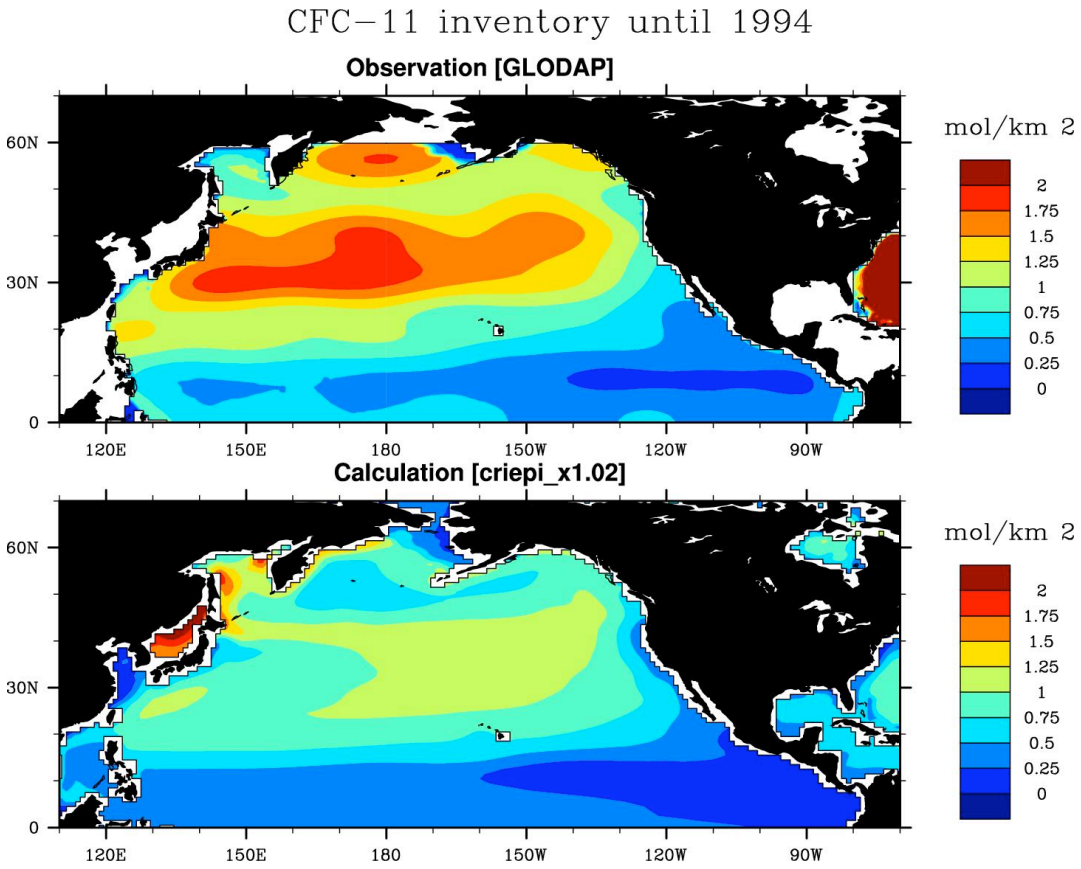

Figure 4. The distribution of CFC-11 water column inventory in the North Pacific for 1994 based on a) GLODAP gridded analysis of field observations [Willy et al., 2004]and b) model simulation.

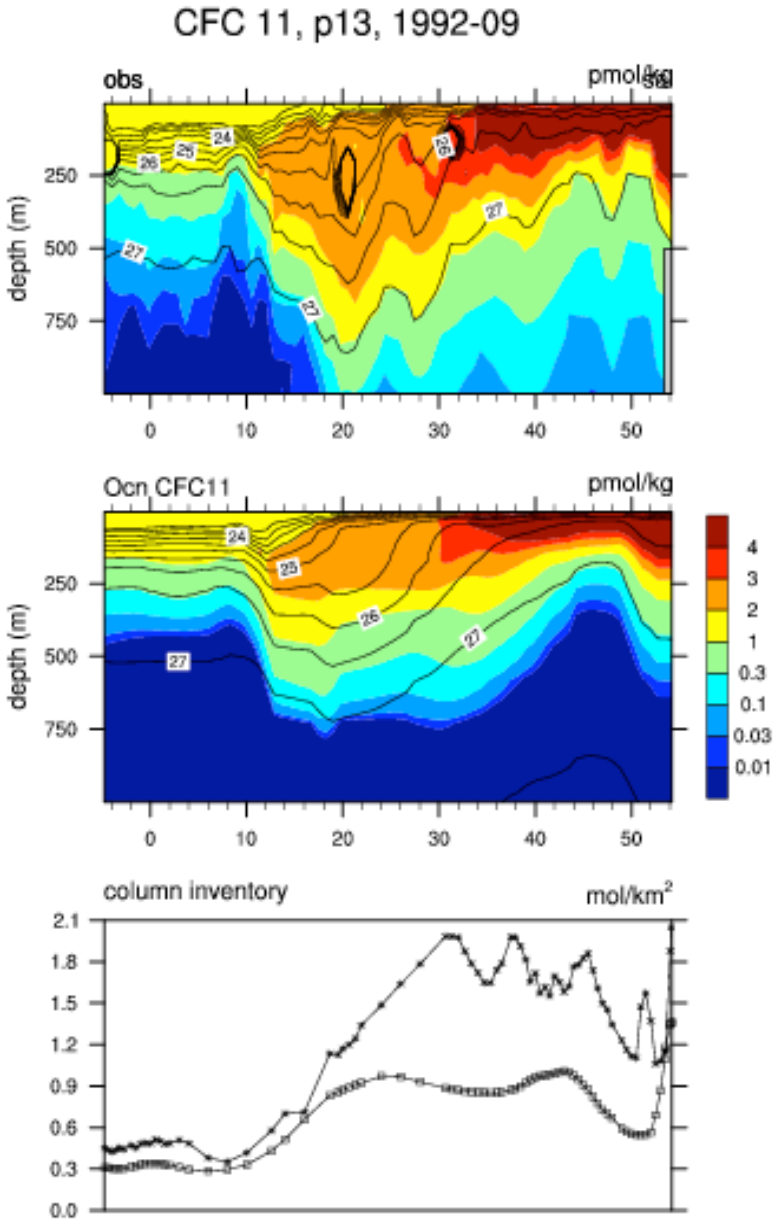

Figure 5. Depth-latitude contour plots of observed (top) and simulated (middle) CFC-11 (pmol kg^{-1}; color contours) along 165˚E meridional section for 1992. Contour lines of the appropriate potential density field are overlaid in black in each panel. The bottom panel displays the model and observed CFC-11 watercolumn inventories as a function of latitude (mol km^{-2}).

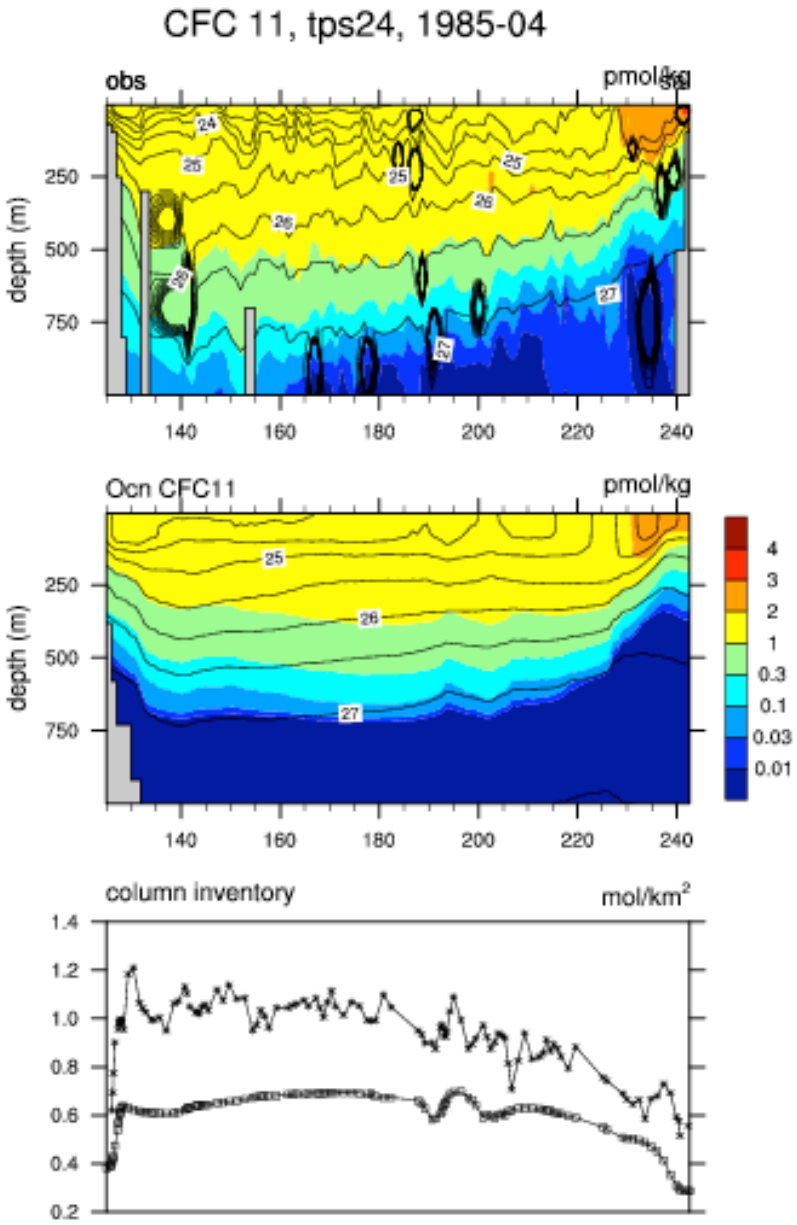

Figure 6. Depth-longitude contour plots of observed (top) and simulated (middle) CFC-11 (color contours) along 24˚N zonal section for 1985. Contour lines of the appropriate potential density field are overlaid in black in each panel. The bottom panel displays the model and observed CFC-11 watercolumn inventories as a function of latitude (mol km^{-2}).

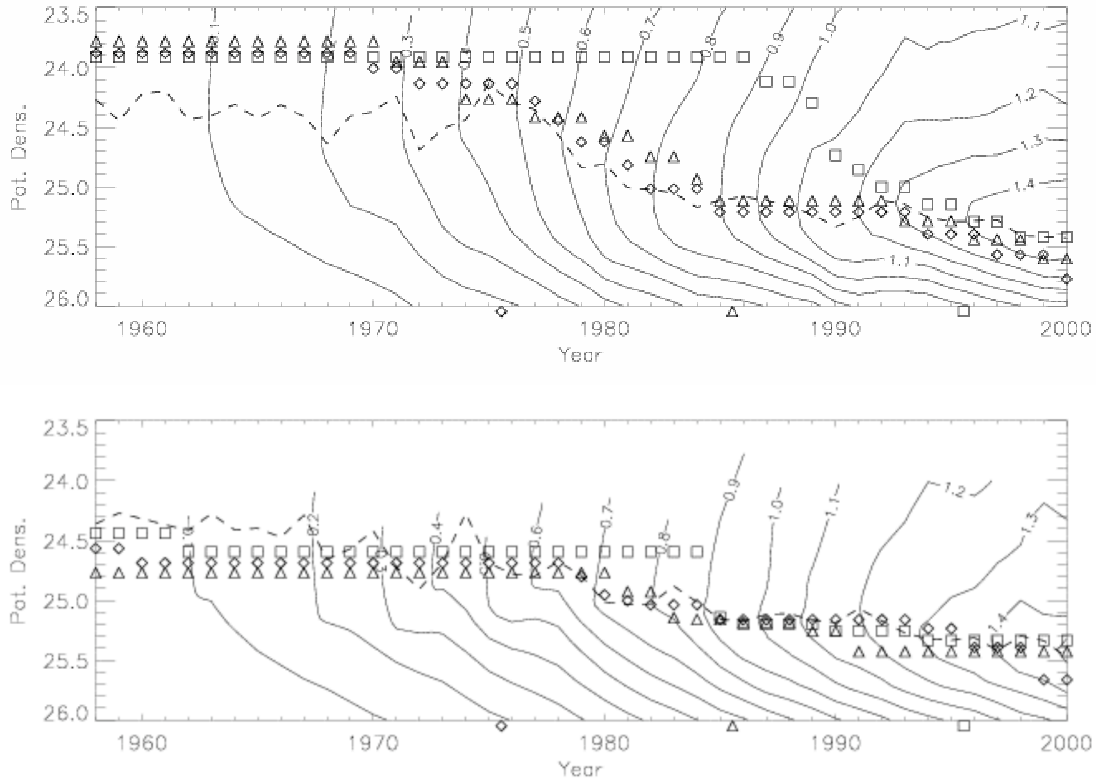

Figure 7. Contour plot of the simulated CFC-12 concentration profile versus potential density at a) 165˚E, 24˚N and b) 140˚W, 24˚N. Dash line shows the calculated depth of the subsurface CFC-12 maximum from the model. Diamonds show the CFC-12 maximum depth from a diagnostic calculation, following the method of Mecking and Warner [2001], using simulated solubilities and pCFC-12 ages from model year 1976. Triangles and squares show the same results based on model year 1986 and 1996 data, respectively.

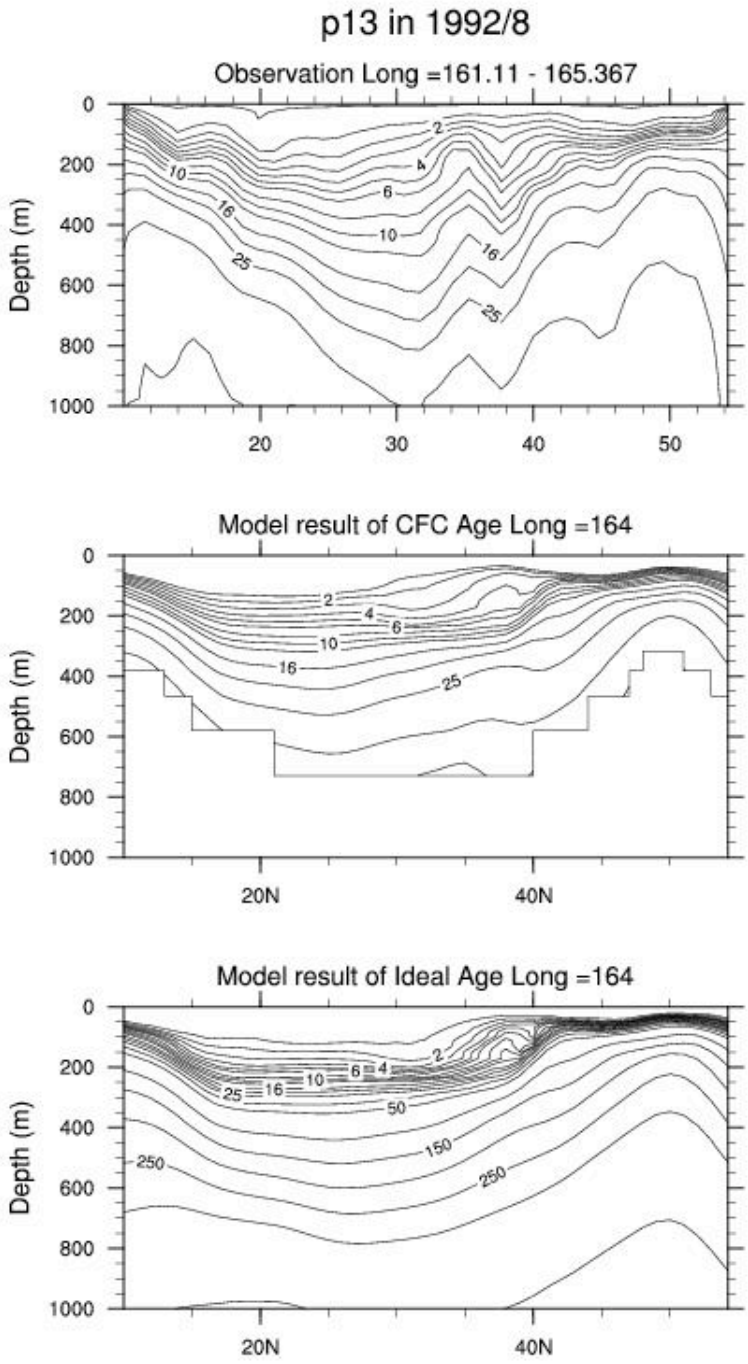

Figure 8. Depth-latitude contour plots of observed pCFC-12 age (top), simulated pCFC-12 age (middle), and simulated ideal age (bottom) along 165˚E meridional section for 1992. All tracer ages are shown in years.

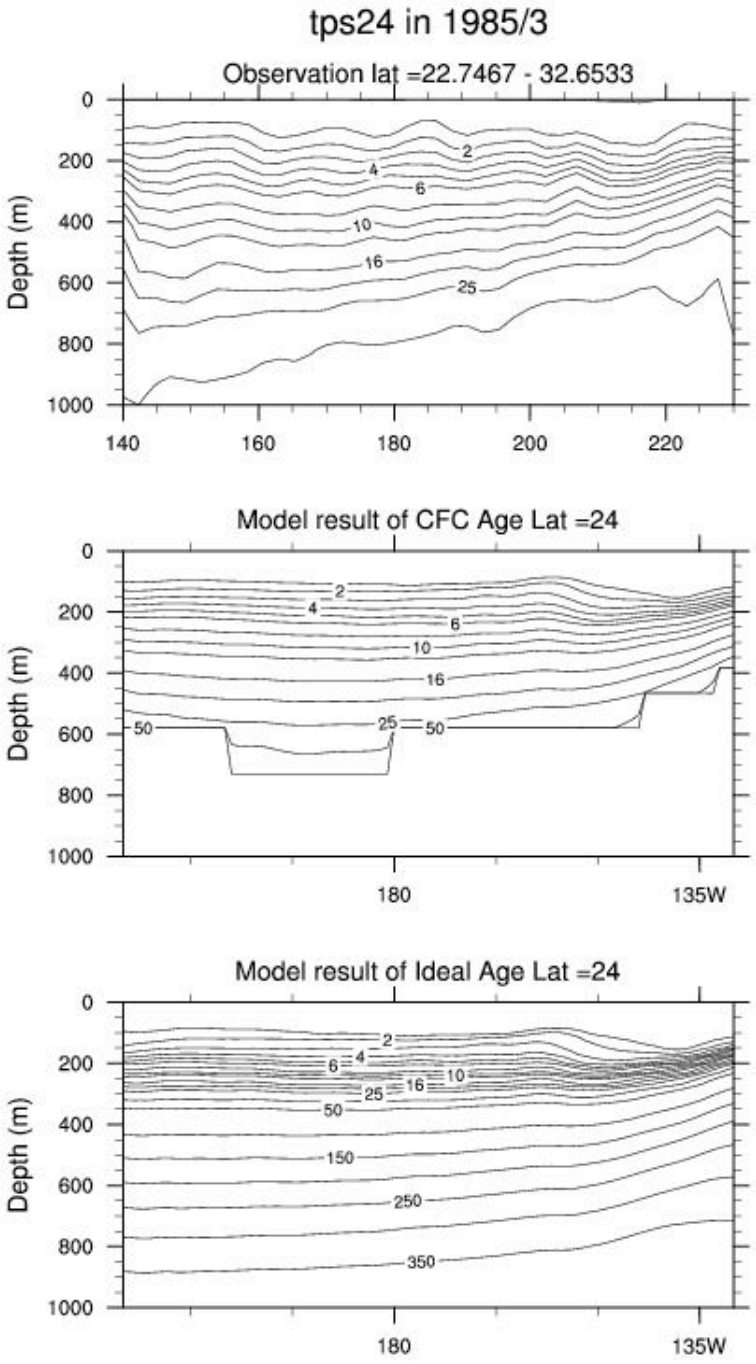

Figure 9. Depth-longitude contour plots of observed pCFC-12 age (top), simulated pCFC-12 age (middle), and simulated ideal age (bottom) along 24˚N zonal section for 1985. All tracer ages are shown in years.

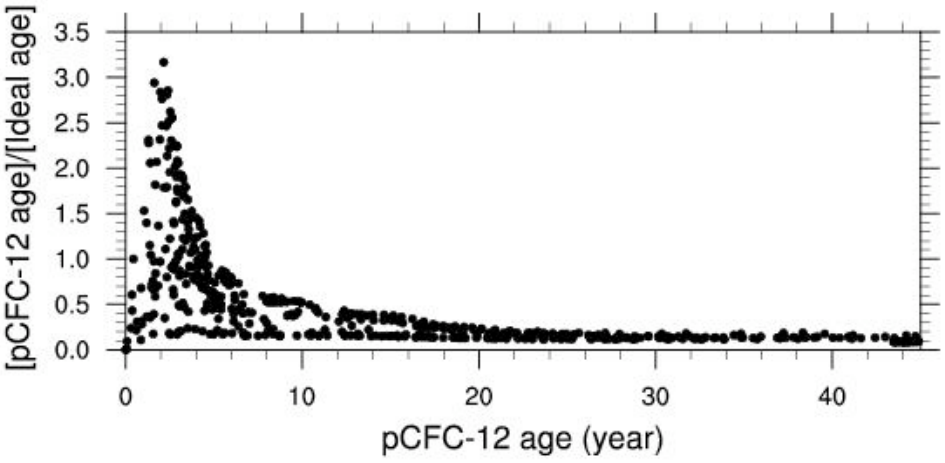

Figure 10. The ratio [pCFC-12 age/ideal age] as a function of pCFC-12 age along 165˚E in 1992 from the simulation.

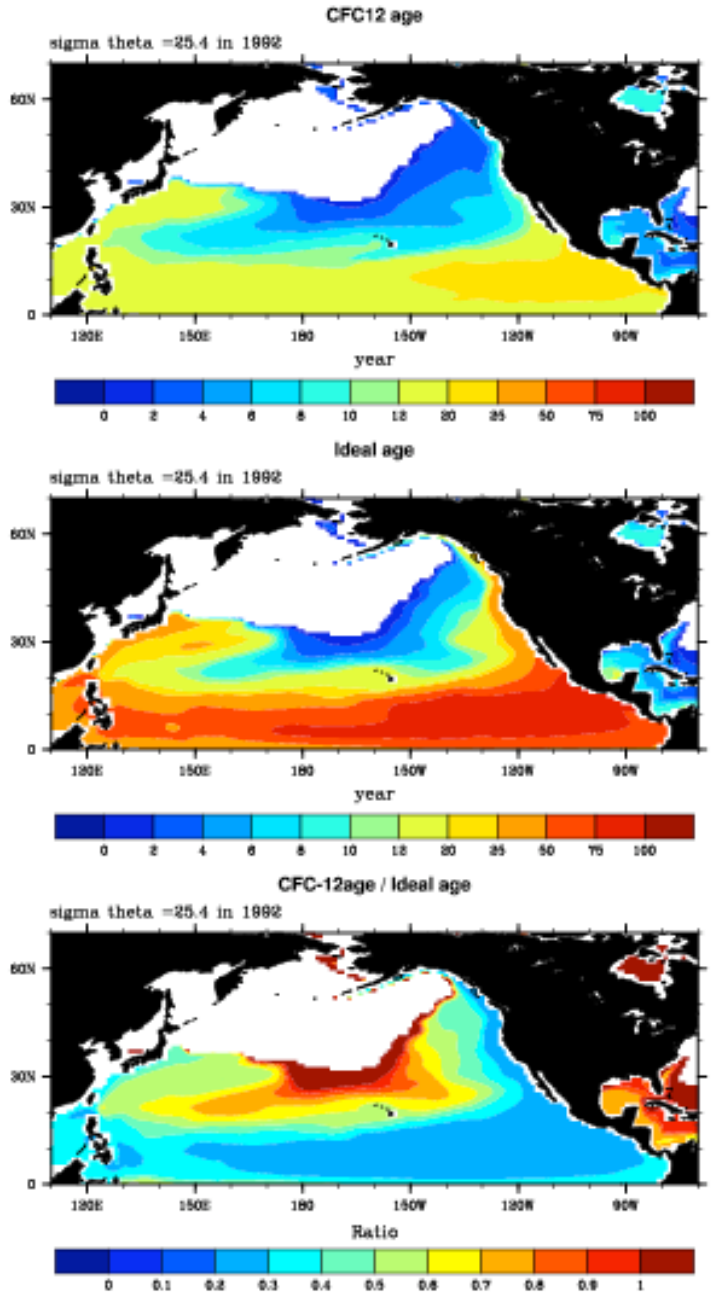

Figure 11. The horizontal distribution of simulated pCFC-12 age, ideal age, and the ratio of pCFC-12 age/ideal age in March 1992 on σ_θ=25.4.

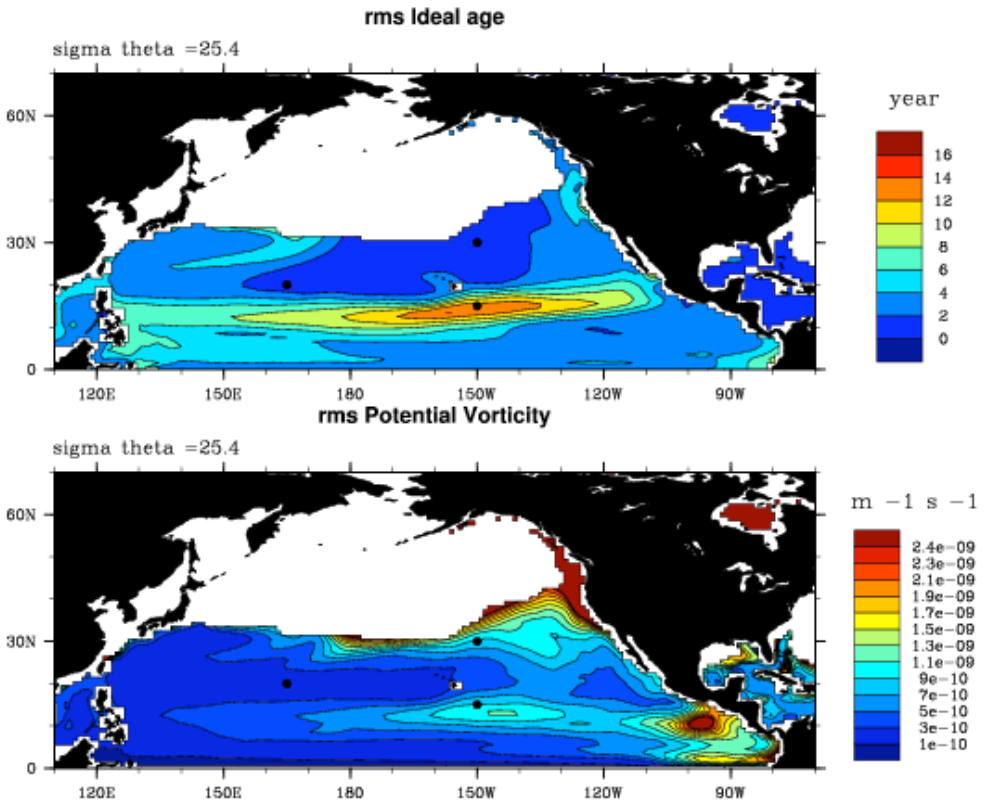

Figure 12. RMS variability in simulated ideal age (top) and potential vorticity (bottom) on σ_θ=25.4 for the period 1958-2000.

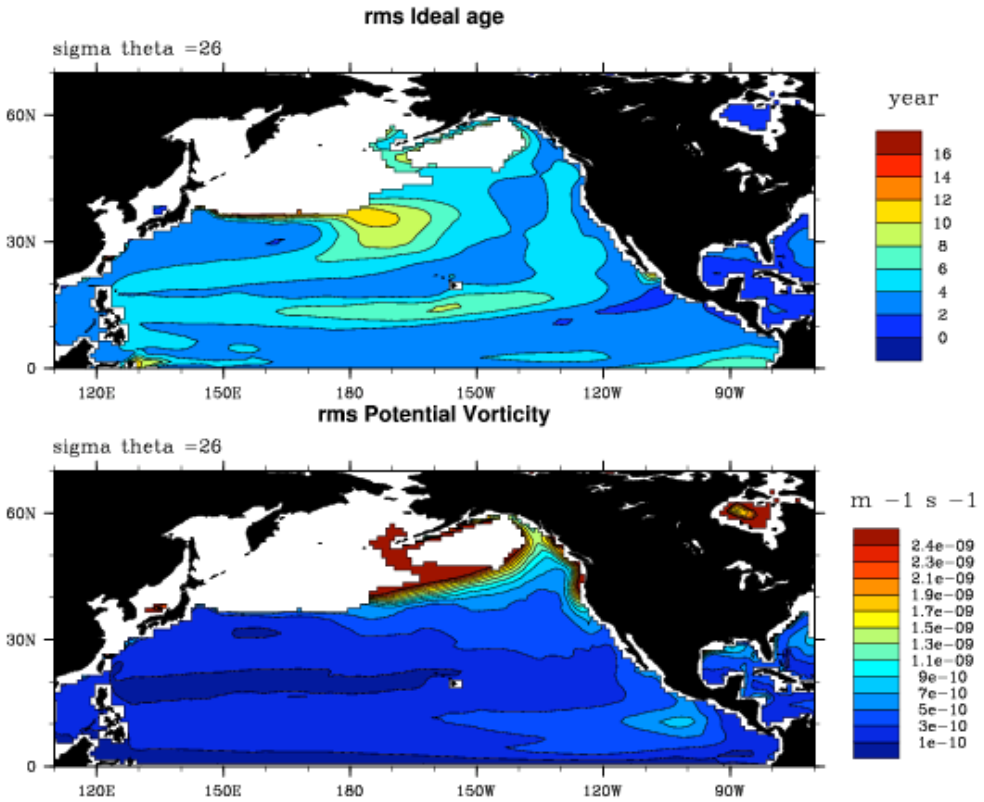

Figure 13. RMS variability in simulated ideal age (top) and potential vorticity (bottom) on σ_θ=26 for the period 1958-2000.

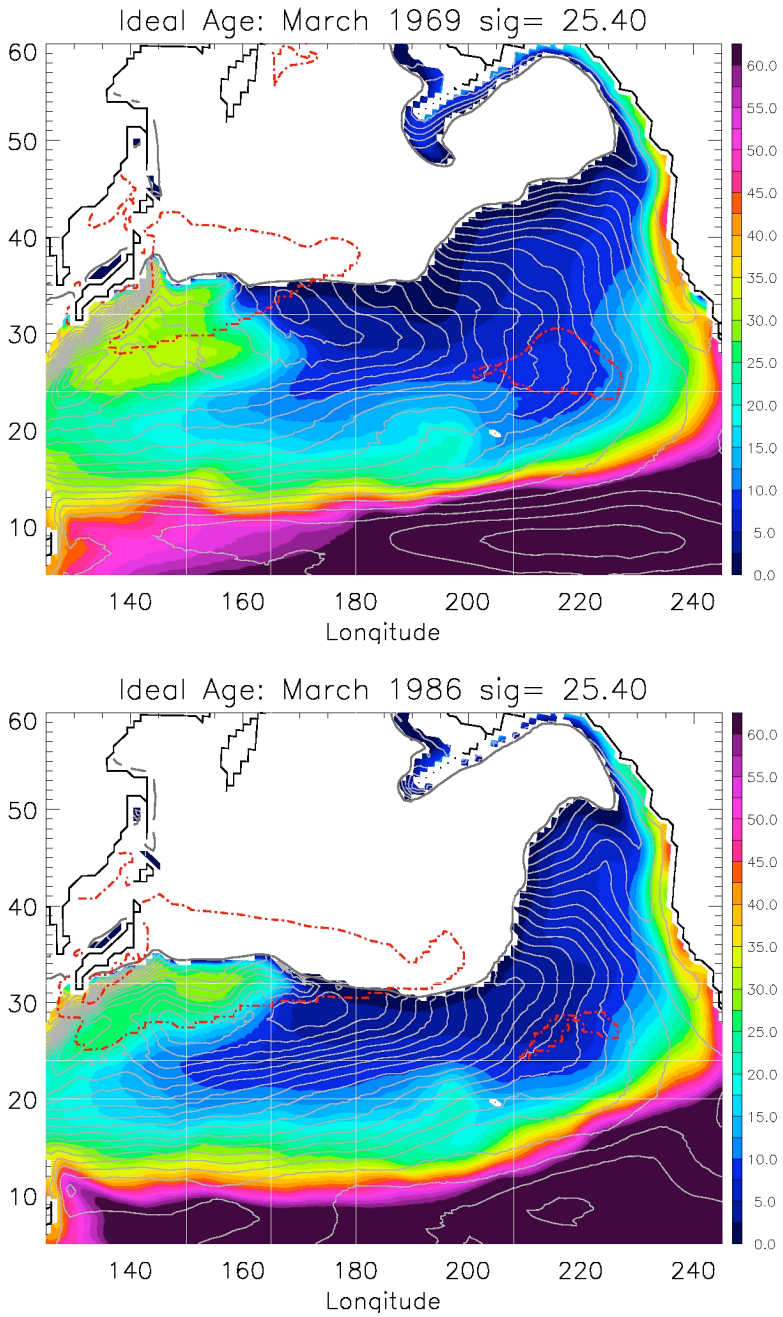

Figure 14. Distribution of simulated ideal age on the σ_θ=25.4 surface in a.) March 1969 and b.) 1986. Ideal age is indicated by color contouring. White contour lines show the Montgomery potential. The heavy red dashed lines show the regions where the mixed layer depth exceeds 150m. The heavy gray contour is the position of the outcrop.

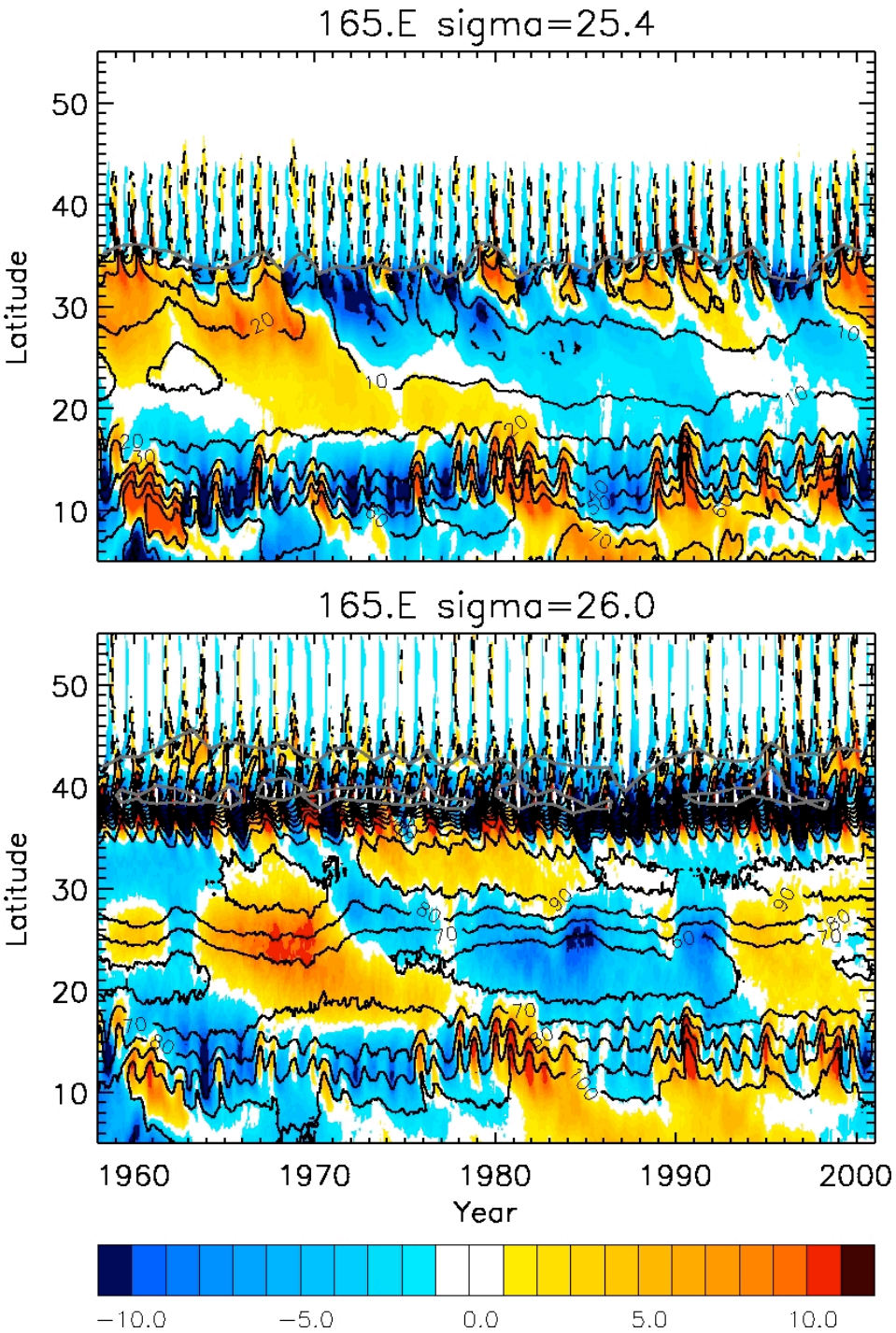

Figure 15. Variation of ideal age along 165˚E on the a.) σ_θ=25.4 and b.) σ_θ=26.0 isopycnal surfaces. Ideal age is shown by black contours, and the difference from the 1958-2000 time mean is shown as color contours. The heavy grey line indicates the latitude of the winter outcrop.

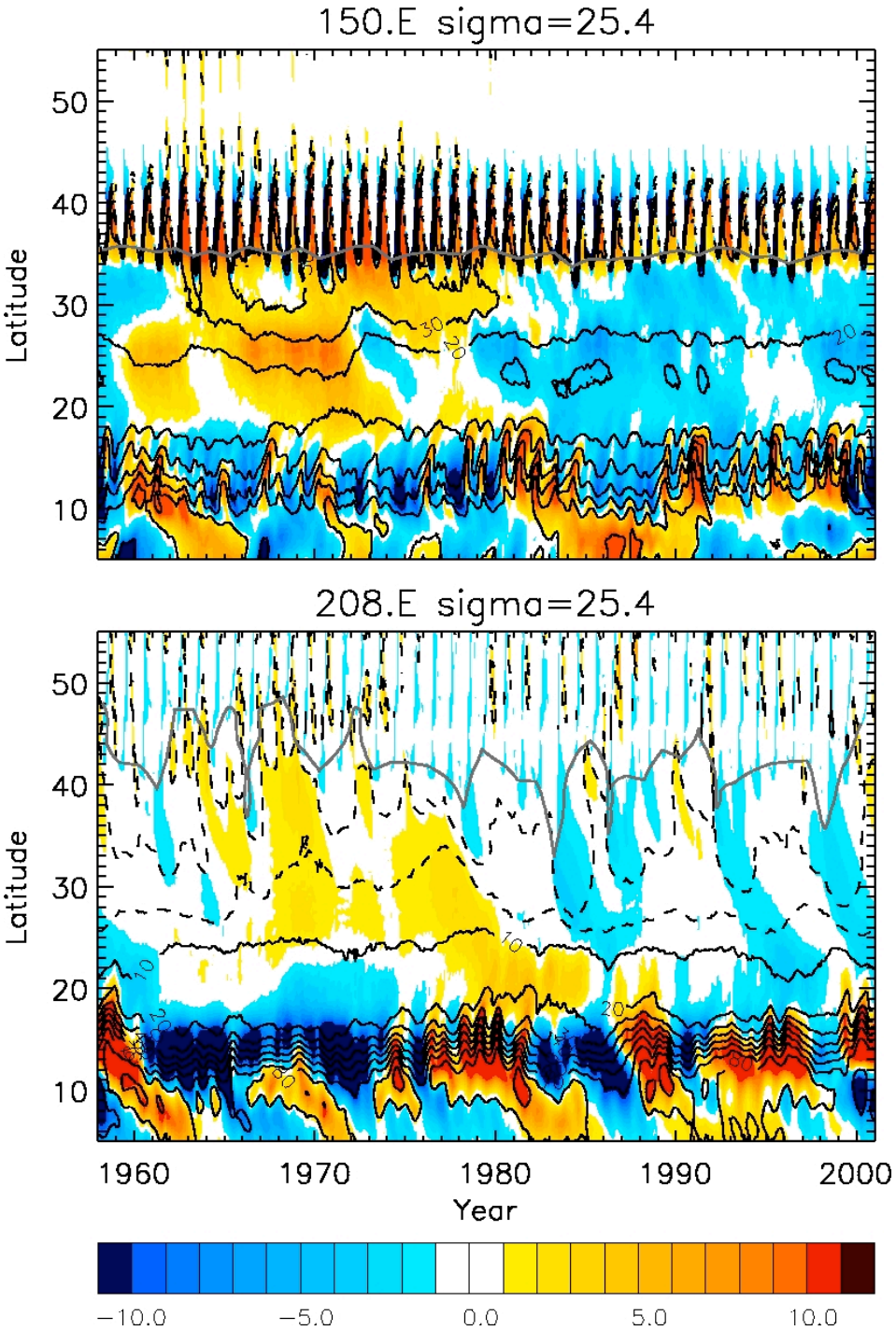

Figure 16. Variation of ideal age on σ_θ=25.4 isopycnal surface along a.) 150˚E and b.) 152˚W. Ideal age is shown by black contours, and the difference from the 1958-2000 time mean is shown as color contours. The heavy grey line indicates the latitude of the winter outcrop.

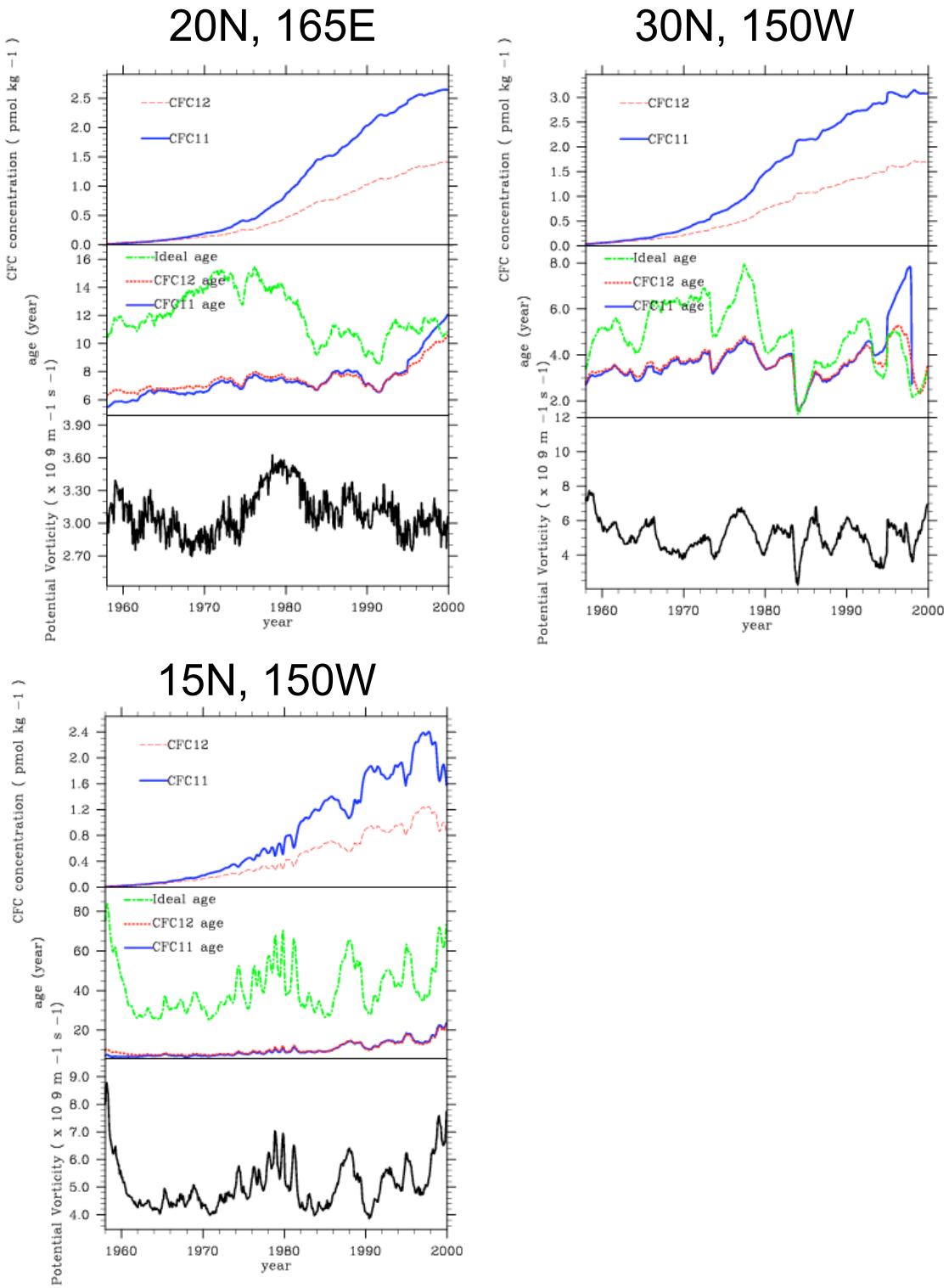

Figure 17. Time series of CFC-11 and CFC-12 concentration (top), ideal age, pCFC-11 age, and pCFC12 age (middle), and potential vorticity (bottom) on the σ_θ=25.4 isopycnal surface at: a) 20°N, 165°E b) 30°N, 150°W c) 15°N, 150°W

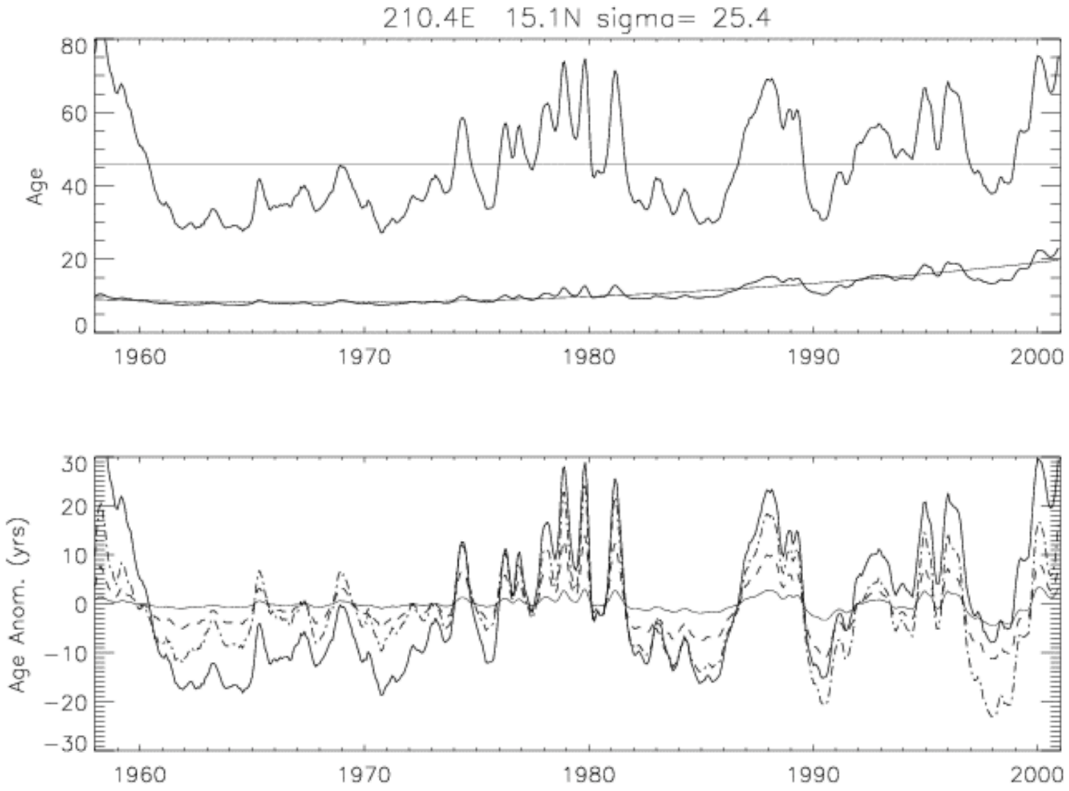

Figure 18. Time series for σ_θ=25.4 isopycnal surface at 150˚W, 15˚N of simulated a) pCFC-12 and ideal age (top) and b) age anomalies (bottom). The mean ideal age and polynomial fit to pCFC-12 age are included in a). The solid line in panel b) shows the anomaly of ideal age. Thin solid line shows the anomaly of pCFC age to the polynomial fit. Dashed curve shows pCFC-12 age multiplied by the ratio of the time mean ideal age to pCFC-12 age and the dash-dot line shows the pCFC12-age multiplied by the ratio of the meridional gradients of the time mean ideal age and pCFC12-age.